


RESEARCH ARTICLE

Sea ice concentration satellite retrievals influenced by surface changes due to warm air intrusions: A case study from the MOSAiC expedition

Janna E. Rückert^{1,†,*} , Philip Rostosky^{1,†}, Marcus Huntemann¹, David Clemens-Sewall², Kerstin Ebell³, Lars Kaleschke⁴, Juha Lemmetyinen⁵, Amy R. Macfarlane⁶, Reza Naderpour⁷, Julienne Stroeve^{8,9,10}, Andreas Walbröl³, and Gunnar Spreen¹

Warm air intrusions over Arctic sea ice can change the snow and ice surface conditions rapidly and can alter sea ice concentration (SIC) estimates derived from satellite-based microwave radiometry without altering the true SIC. Here we focus on two warm moist air intrusions during the Multidisciplinary drifting Observatory for the Study of Arctic Climate (MOSAiC) expedition that reached the research vessel *Polarstern* in mid-April 2020. After the events, SIC deviations between different satellite products, including climate data records, were observed to increase. Especially, an underestimation of SIC for algorithms based on polarization difference was found. To examine the causes of this underestimation, we used the extensive MOSAiC snow and ice measurements to model computationally the brightness temperatures of the surface on a local scale. We further investigated the brightness temperatures observed by ground-based radiometers at frequencies 6.9 GHz, 19 GHz, and 89 GHz. We show that the drop in the retrieved SIC of some satellite products can be attributed to large-scale surface glazing, that is, the formation of a thin ice crust at the top of the snowpack, caused by the warming events. Another mechanism affecting satellite products, which are mainly based on gradient ratios of brightness temperatures, is the interplay of the changed temperature gradient in the snow with snow metamorphism. From the two analyzed climate data record products, we found that one was less affected by the warming events. The low frequency channels at 6.9 GHz were less sensitive to these snow surface changes, which could be exploited in future to obtain more accurate retrievals of sea ice concentration. Strong warm air intrusions are expected to become more frequent in future and thus their influence on SIC algorithms will increase. In order to provide consistent SIC datasets, their sensitivity to warm air intrusions needs to be addressed.

Keywords: Microwave remote sensing, Sea ice, Arctic, MOSAiC, Snow, Warm air intrusions

1. Introduction

The frozen blanket of the Arctic Ocean—the Arctic sea ice—controls fluxes of heat, moisture, and momentum between ocean and atmosphere. Arctic sea ice is also a habitat for marine organisms. As the Arctic has warmed rapidly over the last decades, this component of the

cryosphere has been strongly affected, with a multitude of consequences both locally and outside of the Arctic (Semmler et al., 2012; Fox-Kemper et al., 2021). Since 1979, the September Arctic sea ice extent declined by about 13% per decade (Perovich et al., 2017; Meier and Stroeve, 2022).

¹ Institute of Environmental Physics, University of Bremen, Bremen, Germany

² Thayer School of Engineering, Dartmouth College, Hanover, NH, USA

³ Institute for Geophysics and Meteorology, University of Cologne, Cologne, Germany

⁴ Alfred-Wegener-Institut Helmholtz-Zentrum für Polar und Meeresforschung, Bremerhaven, Germany

⁵ Space and Earth Observation Centre, Finnish Meteorological Institute, Helsinki, Finland

⁶ Institute for Snow and Avalanche Research SLF, Davos, Switzerland

⁷ Eidg. Forschungsanstalt für Wald, Schnee und Landschaft WSL, Birmensdorf, Switzerland

⁸ University of Manitoba, Winnipeg, Manitoba, Canada

⁹ University College London, London, UK

¹⁰ National Snow and Ice Data Center, Cooperative Institute for Research in Environmental Sciences, University of Colorado at Boulder, Boulder, CO, USA

[†] These authors contributed equally to this work.

* Corresponding author:
Email: janna.rueckert@uni-bremen.de

1.1. Sea ice concentration retrievals

Observations from satellite microwave radiometers provide a more than 40-year-long time series of Arctic sea ice area (Spreen and Kern, 2017), giving main insights for sea ice research and providing findings for climate research (Meredith et al., 2019). Retrievals of sea ice concentration (SIC; i.e., the percentage of an ocean area covered by sea ice) using passive microwave sensors take advantage of the different emissions of ice and ocean measured as brightness temperatures by the satellite. Microwave emission from open water depends mainly on surface temperature and surface roughness related to wave and foam formation. The microwave emission of the snow-ice system, on the other hand, depends on snow and sea ice properties such as density, temperature, salinity, stratification, and microstructure. Retrieval algorithms are either (i) based on polarization difference, (ii) combine different frequencies at the same polarization, or (iii) use both different polarizations and frequencies. Overviews and inter-comparisons of different retrieval algorithms are given, for example, in Andersen et al. (2006; 2007), Ivanova et al. (2015), and Kern et al. (2022). In this case study, involving two moist and warm air intrusions in April 2020, we have investigated the performance of common SIC retrievals of type (i) and (iii).

1.2. Warm air intrusions and surface glazing

Moist warm air intrusions transporting water vapor poleward play an important role in the Arctic climate system. They increase the downward longwave radiation flux and the skin temperature and thus contribute to Arctic warming in winter (Woods et al., 2013; Hao et al., 2019). There is evidence for an increase in the frequency of extreme warming events, atmospheric rivers, and cyclones in the central Arctic in winter related to an increase in meridional heat and moisture transport (Woods and Caballero, 2016; Graham et al., 2017; Rinke et al., 2017; Hao et al., 2019; Henderson et al., 2021; Valkonen et al., 2021; Zhang et al., 2023). We refer to these events as “warm air intrusions” in the following, acknowledging that for specific events they can be different, for example, in terms of moisture. Warm air intrusions and associated wind and temperature changes can alter the SIC by ice advection, breaking the ice and opening leads, or, to a lesser degree, by melting the ice (mainly in connection with upwelling of warmer, e.g., Atlantic, water along the ice margins but also by direct melting of the ice surface). However, warm air intrusions can also significantly influence the atmosphere and the surface in ways that alter satellite-measured microwave brightness temperatures (TB; Liu and Curry, 2003).

These alterations can cause spurious changes in SIC products based on TB (Tonboe et al., 2003), that is, they can cause wrong ice concentration retrievals in some cases. One possible effect on the snow surface is surface glazing. By glazing we mean the formation of a thin ice layer or crust on top of the snow due to melt or precipitation (Stroeve et al., 2022) or other mechanisms, for example, winds, as observed in Antarctica (Scambos et al., 2012). Onstott et al. (1987) found that a crust reduces emissivity at 37 GHz and 94 GHz significantly

because of scattering within this layer. Smith (1996) and Comiso et al. (1997) conjectured that ice layers in the snow can be a reason for an underestimation of ice concentration, referring to Mätzler et al. (1984). Mätzler et al. (1984) showed that ice layers introduce interfaces with different refractive indices, affecting especially the horizontally polarized TB close to the Brewster angle as described by the Fresnel equations, and therefore alter the polarization difference. Rees et al. (2010) also observed this effect due to ice lenses on snow on land in the Arctic.

1.3. Multidisciplinary drifting Observatory for the Study of Arctic Climate

Changes in occurrences of surface glazing events thus have the potential to introduce biases in (regional) SIC trends if they are not accounted for. Opportunities to study and quantify the impact of surface glazing in the central Arctic are rare, but the Multidisciplinary drifting Observatory for the Study of Arctic Climate (MOSAiC) expedition (Nicolaus et al., 2022; Rabe et al., 2022; Shupe et al., 2022) provided such a unique setting. To study and increase the understanding of the various processes that lead to the strong recent changes in the Arctic climate, MOSAiC was conducted for a full year from October 2019 to September 2020. The research icebreaker R/V *Polarstern* (Knust, 2017) was moored to a sea ice floe and drifted with it. During the campaign ship-based, ground-based, and airborne measurements of the ocean, sea ice, atmosphere, biogeochemistry, and ecosystem in the vicinity of the ship were collected.

The area within about 2 km of *Polarstern*—named the Central Observatory (CO)—was studied intensively. At the start of the expedition, the CO was on second-year ice with low ice salinities in the upper layers. Due to new ice formation during winter, a mixture of dominating second- and first-year ice prevailed on the scale of satellite footprint.

1.4. Warm air intrusions in April 2020

After a long period of cold winter conditions, two warm and moist air intrusions in April 2020 dramatically warmed the CO (Shupe et al., 2022). During these warm air intrusions, air temperatures increased by up to 30 K at the MOSAiC site, getting close to and even above 0°C. The atmospheric events included record-breaking total water vapor (Rinke et al., 2021) and high cloud liquid water path, increased wind speeds and precipitation, as well as changes in the aerosol regime (Dada et al., 2022) and triggered surface snow metamorphism, that is, transformation processes altering the snow microstructure. Of particular interest here is the large-scale surface glazing, observed at the MOSAiC CO, which can affect the microwave emissions as described above. Before, during, and after the warm air intrusions, the actual SIC in the vicinity of MOSAiC was high (>95%). Single leads opened during the events but nothing major in comparison to the periods before and after as confirmed by optical (MODIS) and radar (Sentinel-1) satellite data, by observations from the expedition participants, and by helicopter-borne thermal infrared imagery (Thielke et al., 2022). The latter gives a value for lead fraction, that is, fraction of open water and

thin (<30 cm) young ice, which was on the order of 1.5% over the CO on April 23, about three days after the intrusions. Still the warm air intrusion events affected satellite products of SIC based on microwave radiometry. In conjunction with the warming events, and lasting for several days after them, most satellite products showed a (wrong) decrease in SIC and inter-product variability increased.

In this study, we examined differences between several satellite ice concentration products during the April 2020 warm air intrusions. To explain the differences, we investigated the effect of these events on microwave TB. We present the suite of such observations at *Polarstern* by satellite and ground-based radiometers on the ice floe measuring at the same frequencies (6.9 GHz, 19 GHz, and 89 GHz). We used in-situ snow and ice observations and microwave emission modeling to explore the impacts of glazing and snow metamorphism on TB and, consequently, on SIC retrievals. The results are structured by the different scales of the observations, from a satellite view (Section 3.1) via a floe-wide perspective (Section 3.4) to a specific on-ice site (Section 3.5), investigating the ground-based radiometer observations taken at the Remote Sensing Site during MOSAiC.

2. Data

2.1. Sea ice concentration: Satellite products

In this section we compare SIC around *Polarstern* based on different algorithms developed for satellite passive microwave remote sensing using different frequencies and polarization combinations. The datasets used are described in more detail in the following subsections. **Table 1** provides an overview including the frequency channels that are used to compute SIC and the grid spacing. All products are available daily. The co-location procedure is the same for all products. In order to account for drift we use *Polarstern*'s position resampled to hourly values and then choose the closest grid point in the satellite product for each hour. We then averaged over the whole day. Note that the ASI SIC product has a higher spatial resolution compared to the others. It can thus be considered more representative of the local ice conditions.

2.1.1. ASI SIC algorithm

The ASI algorithm exploits the high spatial resolution of near 90 GHz channels and was initially developed for

Table 1. Summary of sea ice concentration products used

Algorithm/ Product	Frequencies	Grid Spacing (km)	Sensor
ASI	89V, 89H	6.25	AMSR2
NSIDC NASA Team	19.35V, 19.35H, 37V	25	SSMIS
NSIDC CDR	19.35V, 19.35H, 37V, 37H	25	SSMIS
OSI SAF iCDR	19.35V, 37V, 37H	25	SSMIS

SSM/I sensors (Svendsen et al., 1987; Kaleschke et al., 2001). It was later adapted for the AMSR-E and AMSR2 sensors (Sprenn et al., 2008; Melsheimer, 2019). The polarization difference (PD), described as

$$PD = TB_V - TB_H, \quad (1)$$

where V denotes vertical polarization and H horizontal polarization, at 89 GHz (called PD(89) in the following) is larger over open ocean than over sea ice. This difference is used by the algorithm to distinguish between these two surface types. The SIC is retrieved by a third-order polynomial of PD where the coefficients are determined by the tie points, that is, typical values of PD over water and consolidated ice (100% ice concentration). To correct for weather influences over open ocean, weather filters are applied. Here, we used the dataset operationally available on a 6.25 km grid at <https://seaice.uni-bremen.de> and <https://meereisportal.de>.

2.1.2. NASA Team algorithm

The NASA Team algorithm (Cavalieri et al., 1984; 1997) uses vertically and horizontally polarized TB channels to calculate the polarization ratio, $PR = PD/(TB_V + TB_H)$, of 19.35 GHz, called PR(19) in the following, and the spectral gradient ratio, $GR = (TB_{37V} - TB_{19V})/(TB_{37V} + TB_{19V})$, between TB 19.35V and TB 37V, called GR(37/19) in the following. These two ratios are then compared in a scatter plot where they form clusters. These clusters can be identified as being correspondent to three surface types (first-year ice, multiyear ice, and ice-free ocean), and for each type three constant tie points are determined (for each frequency channel). Values between the tie points are then interpreted as mixtures of surface types. Weather filters are applied additionally to correct for weather influence over open ocean. We used the NASA Team SIC operational product provided as part of the NOAA/NSIDC Climate Data Record of Passive Microwave Sea Ice Concentration, Version 4 (Meier et al., 2021).

2.1.3. NSIDC climate data record

The National Snow and Ice Data Center (NSIDC) provides SIC estimates as a climate data record (CDR) starting in 1978 (Meier et al., 2021). Here, SIC is computed both by NASA Team (see above) and the Bootstrap algorithm (Comiso, 1986; Comiso et al., 2017). The Bootstrap algorithm is based on relationships of TB combinations of 19V and 37V, and 37V and 37H. Clusters of pure surface types are determined in TB scatter plots of these combinations. Tie points are derived daily based on these clusters. Additionally, weather filters are applied. Then, the higher concentration value from the two algorithms is chosen for each grid cell. We used the NSIDC CDR operational product provided by the NOAA/NSIDC Climate Data Record of Passive Microwave Sea Ice Concentration, Version 4 (Meier et al., 2021).

2.1.4. OSI SAF climate data record

OSI SAF global sea ice concentration interim climate data record (OSI SAF iCDR), release 2, provides daily SIC, starting in 2016 and using data from the SSMIS sensors from NOAA CLASS (EUMETSAT Ocean and Sea Ice Satellite

Application Facility, 2017). This SIC dataset, OSI-430-b, is based on a dynamic algorithm (Lavergne et al., 2019), generalizing the Bristol algorithm (Smith, 1996). TB at 19V, 37V, and 37H span a 3-D space. Within this space, clusters or shapes close to lines for closed-ice and water are existent. The algorithm then projects the TB data on an optimized plane. This projection is found using daily updated training datasets, one for fully ice-covered and one for open water areas. The unit vector of this plane is found by principal component analysis (direction of highest variance in brightness temperature) and is then rotated to maximize accuracy. The final SIC is then calculated by a weighted linear combination of SIC computed from an algorithm dynamically tuned to perform better over open water and one dynamically tuned to perform better over high-concentration ice conditions, both applied in the respectively optimized planes in TB space. The TB are corrected using the European Centre for Medium-range Weather Forecasts (ECMWF) ERA-Interim reanalysis data to account for atmospheric influences due to water vapor, wind speed, and near-surface air temperature, with a weather filter (open-water filter) applied after the correction.

2.1.5. Tie points and truncation

All presented satellite products rely on tie points that are average representations of certain ice conditions, for example, 100% SIC. Naturally, this procedure leads to retrievals varying around 100%, including cases with SIC above 100%. The effects of truncating the data at 100% SIC, as done in all presented products (only the OSI SAF iCDR provides additionally non-truncated “raw” data to the users), are discussed in more detail in Kern et al. (2019). They concluded that the NSIDC CDR (note that they used version 3 while we analyzed version 4) systematically overestimates SIC (the non-truncated distribution has a modal value larger than 100%). This overestimation will be of relevance later when we discuss the sensitivity of the presented products to the warm air intrusions.

2.2. Space-borne microwave radiometry: Brightness temperatures

We investigate TB measured by the microwave scanning radiometer AMSR2 on the GCOM-W1 spacecraft from the Japan Aerospace Exploration Agency, launched May 18, 2012. AMSR2 orbits the Earth at an altitude of 700 km in a near-polar, sun-synchronous sub-recurrent orbit with a swath width of 1450 km. The dual-polarized sensor has instantaneous fields of view (FoV) ranging from 62 km × 35 km at 6.9 GHz to 5 km × 3 km at 89 GHz. We used the swath data, both ascending and descending, of the Level 1 R product matched to the resolution of 6.9 GHz (Maeda et al., 2016), corresponding to an instantaneous FoV of 62 km × 35 km. This product matches antenna patterns so that the TB for all frequencies have the same field of view, facilitating comparisons between different frequencies. For every overflight of *Polarstern* we chose the measurement closest to the vessel’s hourly position. There are between five and seven overflights per day. We show daily

averaged values of TB at 6.9 GHz, 18.7 GHz, 36.5 GHz, and 89 GHz in Section 3.1.

2.3. Ground-based microwave radiometry

We focus on two microwave radiometers deployed during MOSAiC observing the surface at 6.9 GHz, 10.7 GHz, 19 GHz, and 89 GHz at horizontal and vertical polarization, similar to AMSR2. The radiometers made observations at incident angles between 35° and 75°. In this study, we show values observed at 45° (6.9 GHz) and 55° (19 GHz and 89 GHz). For this incident angle, the FoV of the radiometers is around 6 m for 19 GHz and 89 GHz and 11 m (H-Pol) to 14 m (V-Pol) for 6.9 GHz. Details are provided in the supplemental Text S1 and Table S1. Due to increased snow accumulation in front of the instruments after the warm air intrusions, the snow was much deeper around the ground-based radiometers compared to the surrounding MOSAiC floe. Especially during and after the second warm air intrusion, deep snow drifts formed in the FoV of some radiometers (Text S2; Table S2; Figures S1, S2, and S3).

2.4. Snow data

Detailed snow measurements were performed during MOSAiC. In this study, we analyzed 132 SnowMicroPen (SMP) profiles (Macfarlane et al., 2021) taken between April 08 and April 27 to support our interpretation of the observed satellite signals. From the raw SMP observations (penetration resistance) snow density and specific surface area (SSA) were estimated using empirical models (Proksch et al., 2015; King et al., 2020). From density and SSA, the exponential correlation length was calculated (see Text S3), a parameter describing the microstructure of the snow which is used in common snow microwave emission models (Tonboe et al., 2006).

2.5. Supporting data

2.5.1. Met Tower temperature

For atmospheric temperature, we used the 2 m air temperature recorded from the 10 m meteorological mast (Met Tower) installed on the CO ice floe (Cox et al., 2021).

2.5.2. Precipitation

To illustrate the timing of precipitation, we used data from the Vaisala Present Weather Detector 22 (PWD22) precipitation gauge, an optical device that was installed on the deck of *Polarstern* and operated by the U.S. Department of Energy Atmospheric Radiation Measurement program (Shi, 2019). Here, we used 1-minute mean precipitation rates. This product was also used as reference product in an inter-comparison of different snow precipitation sensors by Wagner et al. (2022).

2.5.3. Total water vapor from radiosondes

The Level 2 dataset of balloon-borne radiosondes from the MOSAiC expedition (Maturilli et al., 2021) was used to calculate total water vapor (TWV) from the measured temperature, pressure, and relative humidity profiles from the *Polarstern* helicopter deck (at about 10 m height) to about 30 km altitude using the formula for vapor pressure over liquid water below 0°C by Hyland and Wexler (1983) as in

Walbröl et al. (2022). During the warm air intrusions, the radiosondes were launched more often, up to 7 times a day, while during the other periods they were launched 4 times a day.

2.5.4. Liquid water path from HATPRO radiometer

We used liquid water path (LWP) retrieved from the ground-based humidity and temperature profiler (HATPRO) microwave radiometer operated in zenith mode onboard *Polarstern* as input parameter to model the atmosphere. The retrieved LWP is based on the retrieval algorithm as described in Nomokonova et al. (2019) using the vertically polarized TB measurements between 22.24 GHz and 31.4 GHz. The radiometer has a temporal resolution of 1 second. More information on this data set can be found in Walbröl et al. (2022).

2.5.5. Reanalysis ERA5

From ECMWF fifth generation reanalysis ERA5 (Hersbach et al., 2020) we used longwave and shortwave radiation from the grid cell closest to *Polarstern* for the SNOWPACK model simulations (Section 3.3).

2.5.6. Terrestrial laser scanner (TLS)

Supporting information about the snow surface topography was derived from terrestrial laser scan (TLS) data taken on April 17 and April 22 (Clemens-Sewall et al., 2022b). The TLS uses a scanning, 1550 nm laser, to generate a three-dimensional point cloud of the snow and ice surface at centimeter-scale resolution. See Deems et al. (2013) for a review of TLS applications to snow depth measurements. Wind-blown snow particles were filtered out of TLS data using the FlakeOut method (Clemens-Sewall et al., 2022a). From the measured topography and its changes, we deduced the changing snow thicknesses and effective incidence angles (i.e., the incident angle of the tilted surface with respect to the radiometer) within the footprints of the ground-based radiometers. The TLS data also include the backscatter reflectance of the surface at 1550 nm. Glaze ice areas are identifiable in this dataset, because surface glazing reduces the backscatter reflectance (glazing increases forward scattering and absorption).

3. Results

In the following we describe the temporal development of the retrieved SIC and satellite-measured microwave TB, first on a large scale and then locally around *Polarstern*. For the local analysis, we further describe the floe by using the SMP measurements as model input to analyze the evolution of TB. In a second step we change the perspective to an even smaller scale and study the data obtained by the ground-based radiometers. We then discuss the integration of the observations from the different scales. Finally, these steps allow us to develop an interpretation of the satellite signal and the resulting differences in SIC estimates.

Figure 1 shows the temporal evolution of TWV from ERA5 over 4 days. The first intrusion, reaching the ship around April 16, originated in northwestern Russia and

passed the Barents Sea, while the second one around April 19 was approaching from the North Atlantic, illustrating the large area exposed to the warm air intrusions.

3.1. Satellite perspective

The two warm air intrusions were large scale events (**Figure 1**) and thus also visible at large scale in the satellite data. The large scale becomes evident when examining spatial maps of SIC (**Figure 2**). In this figure we show the mean SIC based on different satellite retrieval products for four consecutive days both prior and after the two events and the difference between the two time periods. Note that the SIC from ASI (first row) has a much higher spatial resolution (6.25 km grid spacing compared to 25 km for all other products, see **Table 1**). In all products except for the NSIDC CDR, decreases of SIC are visible in the Central Arctic to different extents (black ovals in **Figure 2**) as well as in the marginal ice zone. The strongest effect is observed for the ASI product, followed by NASA Team. Deviations between different products increased after the events for all products.

The MOSAiC measurements of total water vapor, liquid water path, and 2 m air temperature at *Polarstern* allowed us to examine the effect of these warm intrusions locally. For both warm air intrusions, the rising temperatures (up to 0°C) coincided with increased amounts of TWV (up to 13.4 mm) and LWP (up to around 0.47 mm) as shown in **Figure 3**. In our field observations, no dramatic decrease in ice concentration was observed and SIC was high (>95%), as described earlier in Section 1.4. These findings are also confirmed by SIC derived from satellite thermal infrared data (MODIS instrument, only available for clear sky; not shown). A significant drop in SIC cannot be seen in optical (MODIS) and radar (Sentinel-1) satellite data (not shown) either, where lead formations can be observed during the events but nothing major in comparison to the periods before and after. During the clear-sky day on April 17, temperatures dropped and clear-sky conditions with a high longwave radiation loss prevailed (Rinke et al., 2021). Images from the Panomax webcam onboard the ship (<https://www.mosaic-panorama.org/>) reveal a lead opening close to the ship on that day.

In considering the SIC estimates from different products collocated to MOSAiC, we observe for the high-resolution ASI algorithm based on 89 GHz a drop in SIC between the two warm air intrusions corresponding to the clear sky day on April 17 and a strong decline after the second event (**Figure 3**). The SIC from NASA Team and OSI SAF iCDR shows less variability during the intrusions but decreases in both cases to 92% on April 22 and does not recover thereafter. The NSIDC CDR, on the other hand, shows 100% SIC after the intrusions. This algorithm includes both NASA Team and the Bootstrap algorithm (Section 2.1.3) with the latter compensating for the decrease observed in SIC from NASA Team as discussed later. Before the events, all algorithms showed high SIC around 100%. Similar to the large scale view (**Figure 2**), the spread between different products increased after the events. Using the NSIDC CDR data as reference, we observe SIC differences of around 8% for OSI SAF iCDR

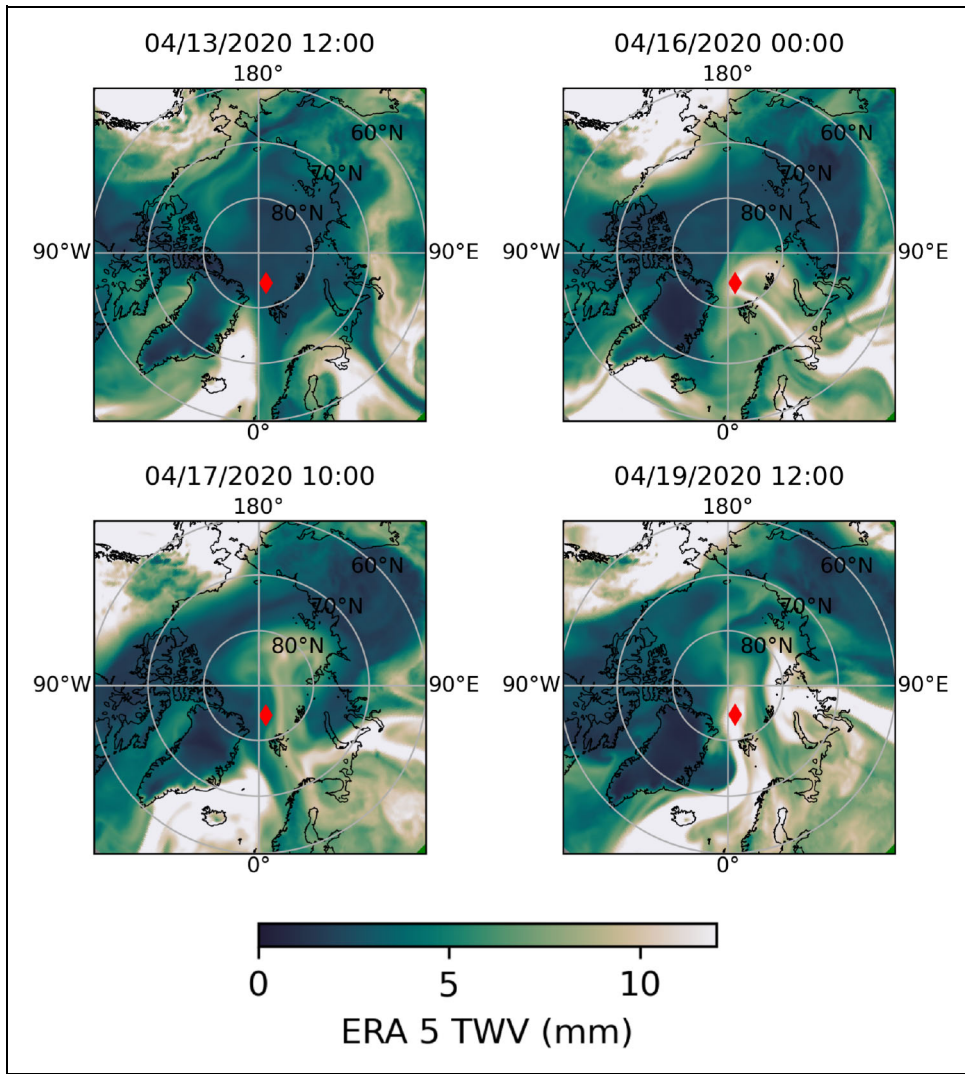


Figure 1. Total columnar water vapor during two warm air intrusion events. Shown are hourly values for total water vapor (TWV) from the reanalysis ERA5. The left panels show TWV one day prior to the events (upper panel) and in-between the two events (lower panel). The right panels show TWV at the time of the first (upper panel) and second (lower panel) warm air intrusion. Dates are month/day/year. The red diamond indicates the position of *Polarstern* at the day.

and for NASA Team. Compared to the higher-resolution ASI product the differences are as high as 34% which cannot be explained by the smaller footprint.

Although Tjernström et al. (2015) observed that warm air advections can cause rapid ice melt, and that dynamic effects can decrease SIC up to 3% in the high SIC domain (Schreiber and Serreze, 2020; Aue et al., 2022), here the low SIC values at MOSAiC retrieved by some algorithms are underestimating the actual sea ice concentration. To understand this underestimation, we analyzed daily satellite AMSR2 TB data (Figure 4b). The signature of the warming events is clearly visible in the TB time series at these frequencies. The higher frequencies (i.e., 36.5 GHz and 89 GHz) follow the 2 m air temperature evolution (Figure 4a) more closely. All frequencies show an increased PD after the events as can be seen in Figure 4c. Again, the higher frequencies show a larger increase. The PD increase on April 22 compared to the mean of April 10–13 ranges from a few Kelvin (approximately 3 K) for 6.9 GHz up to around 9 K

and 11 K for 89 GHz and 36.5 GHz, respectively. A smaller increase in PD at 89 GHz of a few Kelvin (approximately 4 K) is already visible around April 17 between the two warm air intrusions. During the second warm air intrusion, PD for 89 GHz initially decreases, again coinciding with rising TWV and LWP values. After this second event the rise in PD can be observed at all frequencies but most strongly at the higher frequencies. Figure 4d illustrates that both the gradient ratio and the polarization ratio show higher values after the intrusions (after April 20). The gradient ratio shows even higher values during the intrusions.

Especially ASI and NASA Team make use of polarization differences and polarisation ratios, respectively. For such SIC estimates, the changes in these quantities result in (too) low retrieved SIC values as shown in Figures 2 and 3. The decrease of SIC in the high-resolution ASI product on April 17 is possibly real, related to the lead opening described above. Directly relating the effect of these TB changes to SIC from OSI SAF iCDR is not as

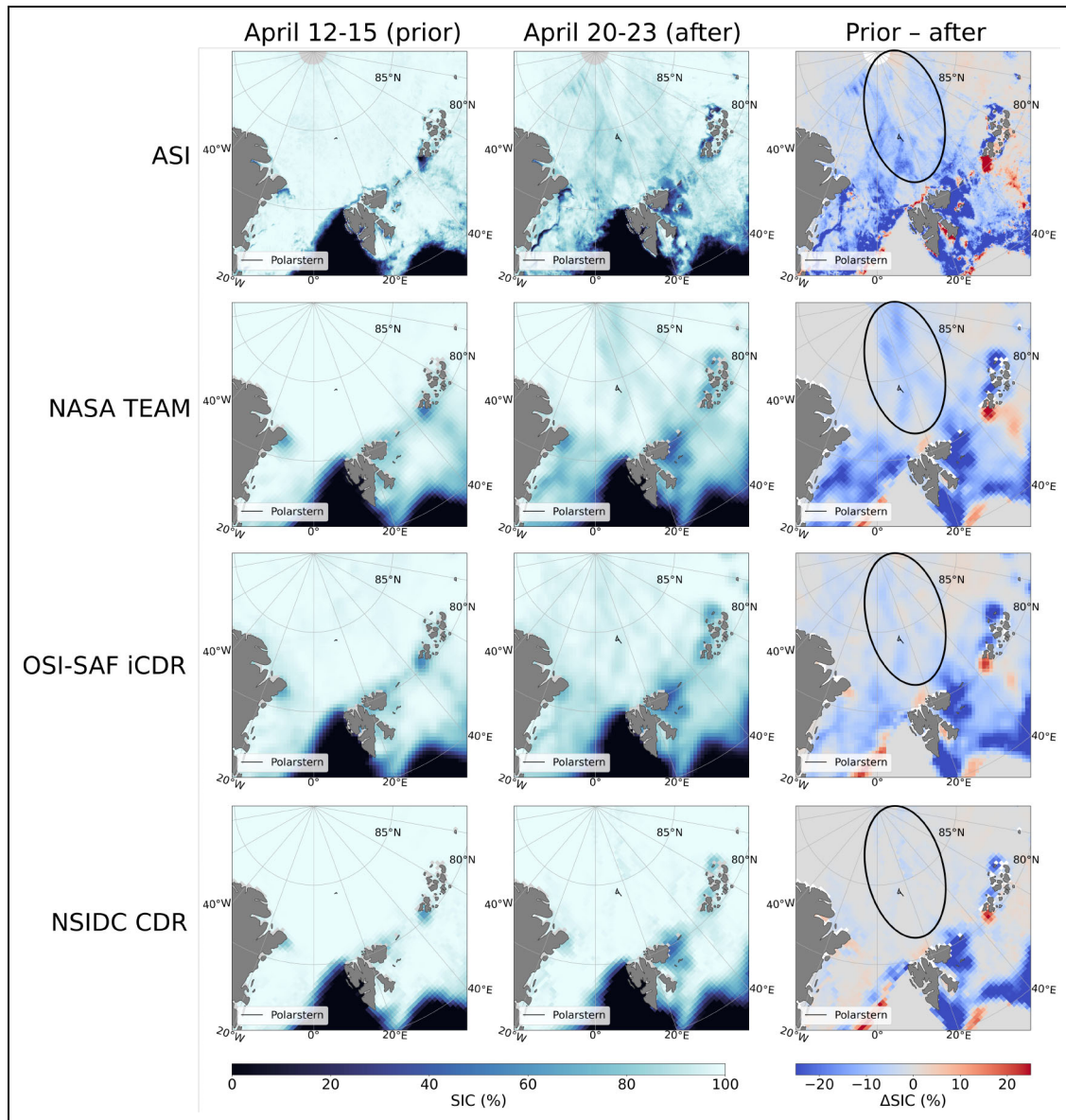


Figure 2. Sea ice concentration from different satellite retrievals before and after two warm intrusion events.

Shown are 4-day averages of sea ice concentration (SIC) prior (first column) and after (second column) the intrusions. The third column shows the difference between the second and first column. Blue colors denote a reduction in SIC after the events. The black oval in the third column marks a region where the different satellite products deviate from each other after the events. *Polarstern's* drift track is shown by a black line.

straightforward due to the complex retrieval method. We note, however, that this algorithm is based on the three-dimensional diagram in TB space of 19V, 37V, and 37H, so that strong changes in these frequencies relative to each other, as observed, will affect the retrieval. The OSI SAF iCDR product provides two uncertainty estimates: algorithm uncertainty and “representativeness” uncertainty, that is, uncertainty due to resampling and mismatch of footprints at different channels (Laverne et al., 2019). Here, the sum of these two uncertainties (given as one standard deviation) increases from below 2% before the events to up to 5.6% on April 21 (not shown) for the co-located data shown in **Figure 3**, that is, the uncertainty estimates identify a potential problem in the retrieved SIC. In this

case, the higher uncertainty is caused by a higher representativeness uncertainty.

For the NSIDC CDR the higher value of the SIC estimates from the Bootstrap algorithm and NASA Team is chosen. The SIC estimate from NASA Team exhibits a decrease as described above, thus the Bootstrap algorithm is responsible for the low sensitivity of the NSIDC CDR SIC estimate to the warm air intrusions. For high ice concentration values as in this case, the Bootstrap algorithm is based on 37V and 37H. However, as described in Section 2.1.5 and discussed by Kern et al. (2019), the fact we do not observe a decrease here, although the relationship of 37V and 37H is changed, might be due to an overestimation and consequent truncation at 100% of the values derived by the Bootstrap algorithm.

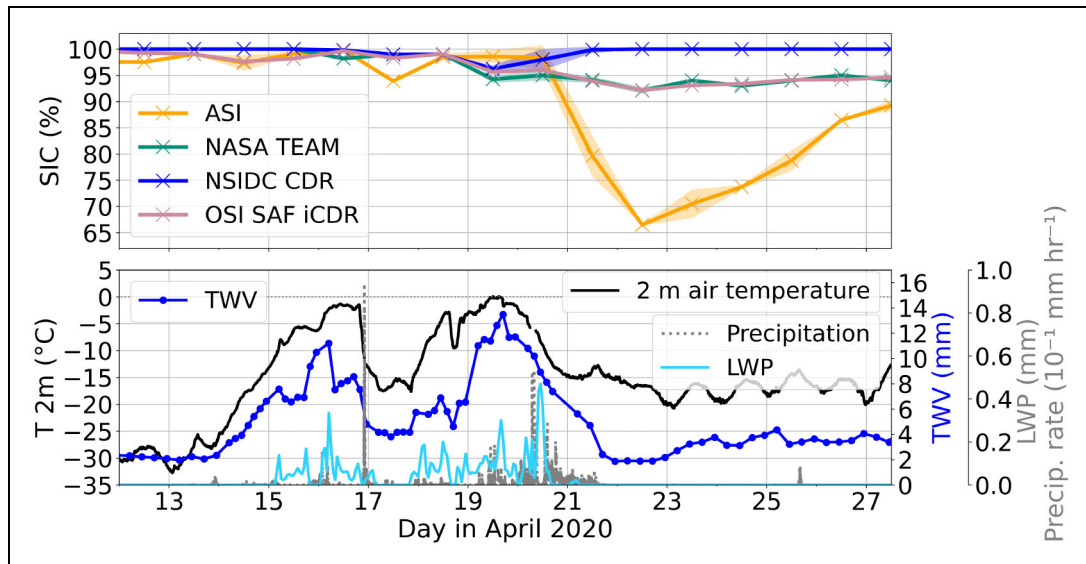


Figure 3. Sea ice concentration and meteorological conditions during the April 2020 warm air intrusion events. Upper: sea ice concentration (SIC) from four different operational satellite products co-located with *Polarstern*. Shown are daily averages at 12:00 UTC on the respective day with the shaded area indicating the standard deviation which is larger zero if the drift of *Polarstern* covered several grid cells. Lower: air temperature at 2 m (black) from the Met Tower, total water vapor (TWV, dark blue) from radiosondes, liquid water path (LWP, light blue) from the HATPRO microwave radiometer (resampled to hourly values), and 1-minute precipitation rates (gray) from the precipitation gauge (PWD22) installed on deck.

3.2. Direct atmospheric influence

In the few days after the warm air intrusions, the 2 m air temperature and TWV were on average higher than before, while LWP was as low as during the first 2 weeks of April (**Figure 3**). Previous studies (Oelke, 1997; Andersen et al., 2007) demonstrated that atmospheric events can also increase retrieved SIC, although we observed a decrease in our case. Emissions from water vapor or liquid water path contributing to the satellite signal are in general not polarized (Ulaby and Long, 2014) and would thus not increase PD. Scattered radiation, for example, by ice particles in clouds, may have a polarized component. However, Troitsky et al. (2003) observed values of PD and duration of periods with polarization differences that are too small to explain the development of PD that we observed here. Also, compared to the surface emissions, the contribution of the atmosphere is small at the low frequencies 6.9 and 19 GHz and thus is not the most likely candidate for the PD increase. Factors other than direct atmospheric effects must explain the increase in PD. We thus focus on explanations related to changed surface emission.

3.3. Snow accumulation and metamorphism

Wagner et al. (2022) described a significant snowfall event from April 16 to April 21 accompanying the warm air intrusions. Snowfall events could have had an increasing effect on PD due to atmospheric scattering, but we observed the increase *after* the snowfall. A detailed analysis suggests that much of the fresh snowfall during this event may have been lost into leads (Clemens-Sewall et al., 2023). According to snow buoy measurements (Nicolaus et al., 2021), the average snow depth on a regional scale

around the MOSAiC floe was around 20 cm until April 20 and 24 cm afterwards (not shown here). If snow accumulates on level ice, we would expect the fresher snow (less dense with refractive index between that of air and ice) to decrease the PD as described by the Fresnel equations and also reported in Hwang et al. (2007) and Tonboe (2010). For the large-scale area, this snowfall cannot explain the microwave signal. The surface conditions at the Remote Sensing Site on the MOSAiC floe were not representative of the larger area, mainly because the instruments themselves posed obstacles that caused artificial snow accumulation. Thus, for the ground-based radiometers the snowfall is relevant to the interpretation (Section 3.5).

For understanding and modeling the observed microwave emission, temperature profiles of the snow are important. Here we have used temperature profiles from simulations with the SNOWPACK model (Bartelt and Lehning, 2002; Lehning et al., 2002a; Lehning et al., 2002b; Wever et al., 2020). The model was initialized with a snow pit from April 08 and driven with MET tower 2 m air temperature and 10 m wind speed. Long wave and short-wave radiation was obtained from ERA5 reanalysis data (Hersbach et al., 2020). In these simulations, snowfall was omitted. At the time the simulations were performed, radiation measurements from MOSAiC were not available. However, we generally found a good agreement between our simulated snow temperature profiles and temperature measurements from snowpits (average difference <2 K) and concluded that the performance of the model is sufficient for the purpose of this study. For simulating the brightness temperature of the snow/ice system of the MOSAiC floe, density and correlation length from the SMP profiles were used (Text S3 and Text S4) together with the

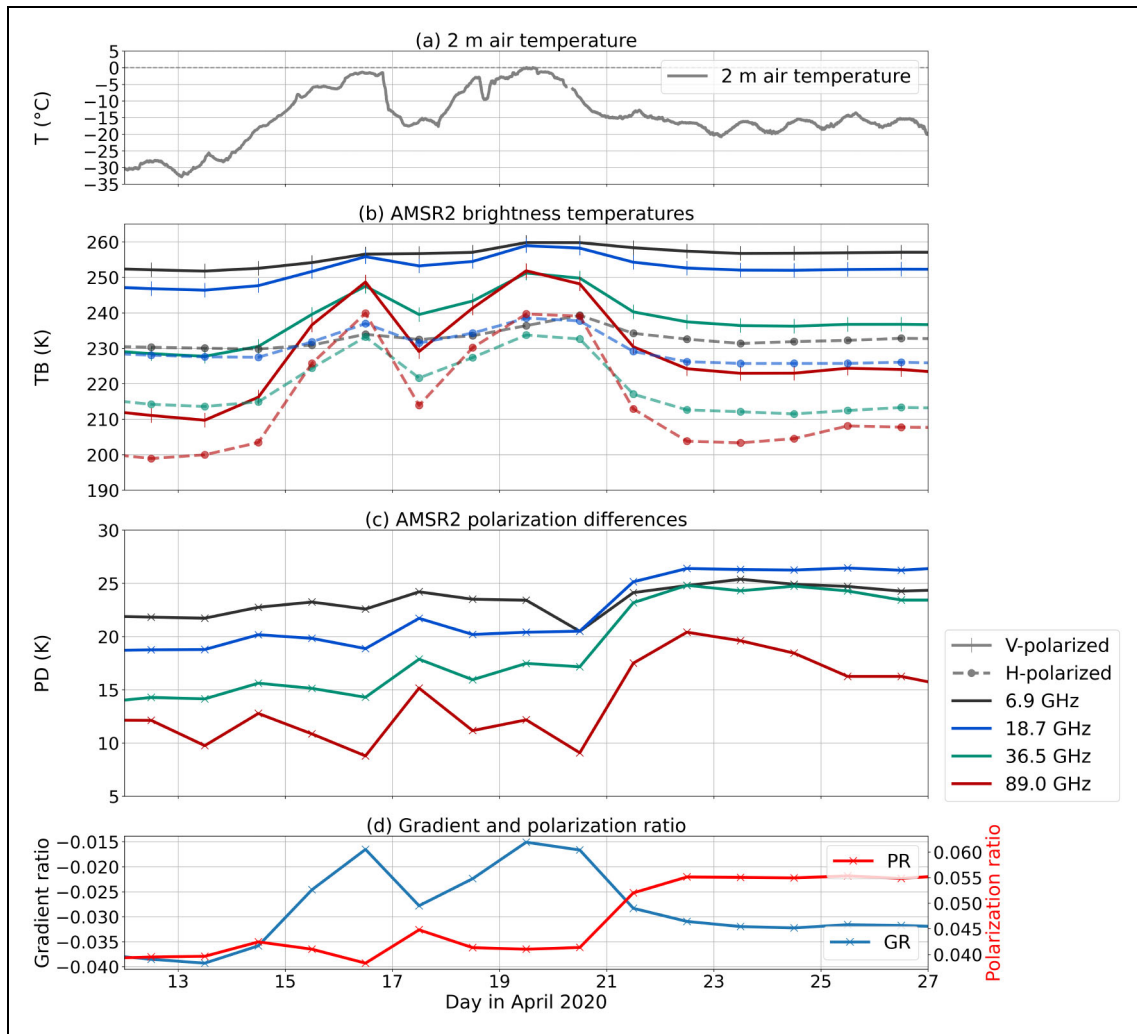


Figure 4. Effect of warm air intrusion on satellite-measured brightness temperatures. Shown are (a) the air temperature at 2 m; (b) the co-located satellite measurement of brightness temperatures (TB); (c) polarization differences (PD) around *Polarstern* (daily averages); and (d) the gradient ratio of 36.5 GHz and 18.7 GHz and polarization ratio of 18.7 GHz as defined in Section 2.1.2.

temperature profiles from the SNOWPACK simulations. To match the varying snow height of the SMP profiles, simulations with a snowpack of 10 cm to 30 cm in 5 cm steps were performed.

Figure 5 shows the simulated snow temperature for a 20 cm deep snowpack. Overall, the snow temperature increased by more than 10 K. After the events, the snow temperature remains higher at the lower part of the snowpack for several days. These data serve as input for the microwave emission modeling presented in Section 3.4.

The changes of the snow microstructure caused by the warm air intrusions are evident when one examines the SMP profiles shown in **Figure 6**. A shift towards lower density and SSA and higher correlation length after the warm air intrusions is visible in the data, suggesting that the warm air intrusions led to snow metamorphism. The strong and even inverted temperature gradient affects the migration of water vapor (deposition and sublimation) in the snow, and we would expect larger snow structures (i.e., depth hoar) resulting in lower SSA, which is indeed visible in the data. The changes in density are mainly in the upper

layers (5 cm) of the snow, which indicates that at least a thin layer of fresh snow accumulated on top of the snow.

The change in increased correlation length affects the scattering strength of the snow: in general higher correlation lengths lead to stronger scattering. On the other hand, higher snow temperatures (**Figure 5**) increase emissions. To understand how these surface changes affect TB in more detail, we modeled the microwave emissions as indicated in the following section.

3.4. Floe perspective: Microwave emission modeling

We further adopted the floe-wide perspective by using a statistical approach in modeling the TB. If we assume that the SMP measurements are representative of the CO (at a length scale of approximately 2 km) in terms of statistical distributions of the measured quantities, we should be able to simulate the effect of the warm air intrusions on the microwave signature. The following simulations were performed with the sea ice version of the Microwave Emission Model for Layered Snowpacks (MEMLS; Wiesmann and Mätzler, 1999; Tonboe et al.,

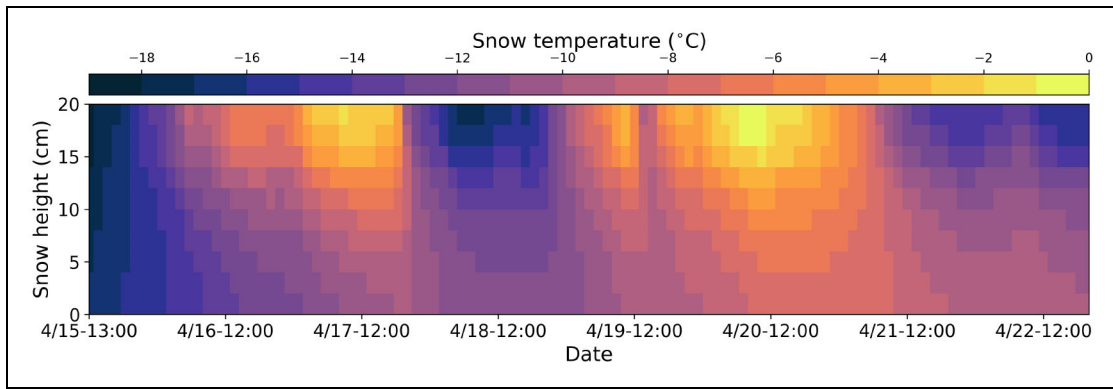


Figure 5. Snow temperature profile from a SNOWPACK simulation initialized with 20 cm of snow. Dates are month/day-hour in 2020.

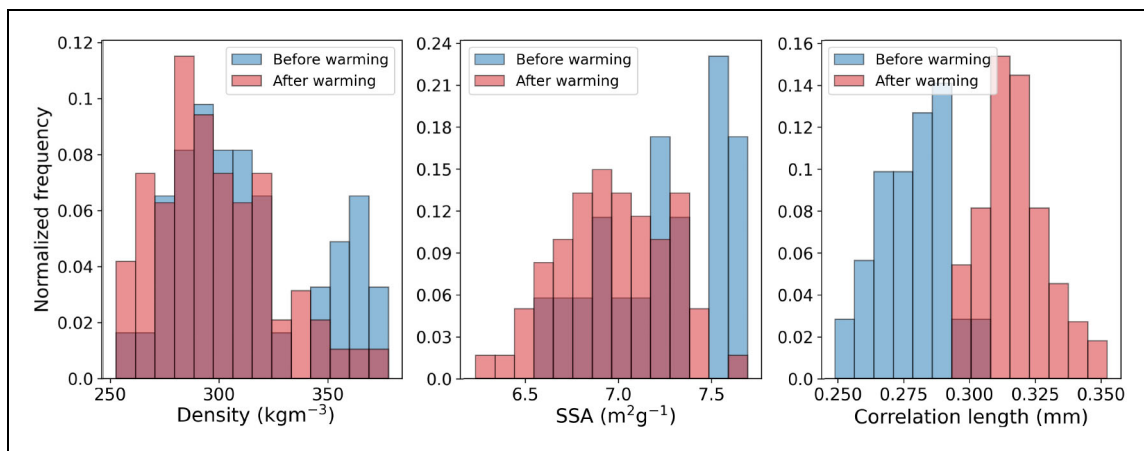


Figure 6. Histogram of average density, specific surface area (SSA), and correlation length of 132 SnowMicroPen profiles. The data are color-coded for the period of April 08–15 (blue) before the warm air intrusions and the period of April 21–27 (red) after the intrusions, and are normalized to 1.

2006). Details about the model setup and initialization are given in Text S3 and Text S4. The simulations were not tweaked to match the satellite observations because we do not consider an atmosphere in our simulations. For the simulations, we assumed a second-year ice floe (Table S3), while on satellite scale, the ice was a mixture of second-year ice and first-year ice. In addition, the snow height might be different on the MOSAiC floe, compared to the surrounding larger area. Consequently, the absolute values presented in the following can differ from what the satellites observe. The focus of the analysis is mainly on a qualitative level.

3.4.1. Brightness temperatures from modeling

In **Figure 7** we show the modeled polarization ratio of 18.7 GHz (PR(19)), the gradient ratio of 36.5 GHz and 18.7 GHz at vertical polarization (GR(37/19)), and the polarization difference at 89 GHz (PD(89)) before and after the warming events. The model output for the individual frequencies is shown in Figure S4. In general, the model output shows a clear increase of TB for all frequencies (at both polarizations) except for 36.5 GHz, where the situation is reversed (Text S4). Qualitatively, an increase

is also seen in the satellite data (**Figure 4**) for all frequencies but the horizontally polarized TB at 18.7 GHz and 36.5 GHz.

When examining the ratios that are used in many SIC algorithms, the polarization ratio at 18.7 GHz remains mostly unchanged in the simulations (upper panels in **Figure 7**). GR(37/19) increases noticeably compared to the values prior to the warming events, and PD at 89 GHz shows only a slight increase. From a satellite perspective we observe an increase in all three quantities (**Figure 8**), which differs from what we observe in the model. Understanding the pronounced rise in satellite-measured PD, which causes the strong drop in SIC from the ASI algorithm, is key for potentially improving such PD-based SIC algorithms. As discussed earlier, the change in PD(89) cannot be explained by variability in downwelling radiation due to cloud cover and thus must be due to changes in the snow surface which, however, are not captured by the quantities derived from SMP profiles (density, SSA and correlation length). In the following, we propose an explanation for the observed changes in brightness temperature including a thin glaze ice layer in our simulations.

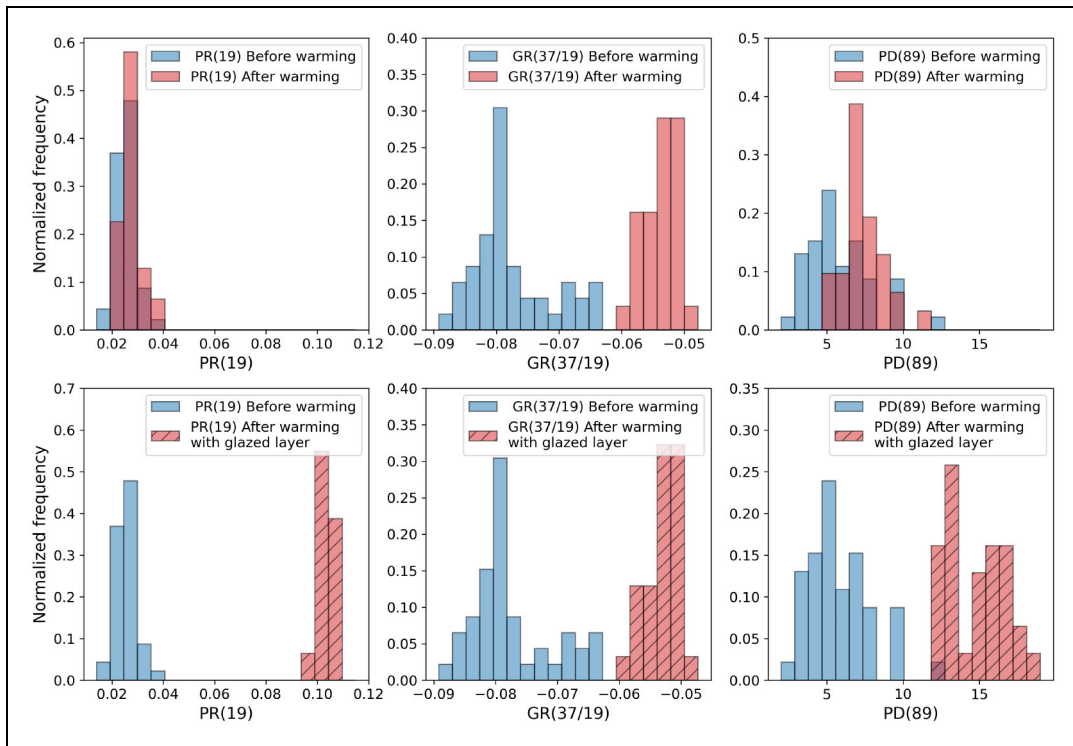


Figure 7. Histogram of simulated polarization ratio, gradient ratio, and polarization difference for 84 SnowMicroPen profiles. The data for polarization ratio, PR(19), gradient ratio, GR(37/19), and polarization difference, PD(89), are color-coded for the period of April 08–15 (blue) before the warm air intrusions and the period of April 21–27 (red) after the intrusions, and are normalized to 1. In the bottom panels, a thin ice layer (2 mm) was added on top of the snow (red, hatched) to simulate the effect of surface glazing after the second warming wave.

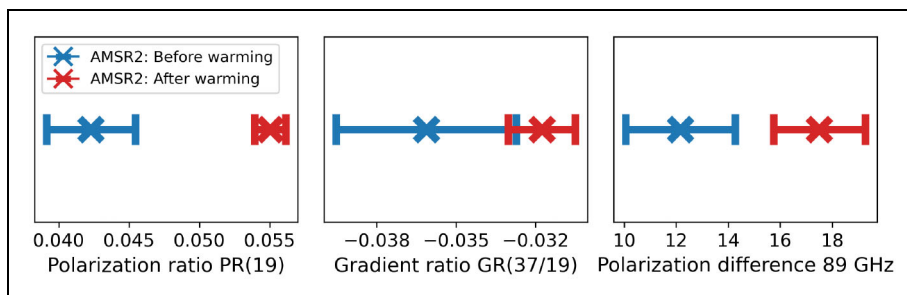


Figure 8. Statistics for polarization ratio, gradient ratio, and polarization difference derived from satellite observations. The mean (\bar{x}) and standard deviation (error bars) for polarization ratio, PR(19), gradient ratio, GR(37/19), and polarization difference, PD(89), are color-coded for the period of April 08–15 (blue) before the warm air intrusions and the period of April 21–27 (red) after the intrusions, matching the modeled periods in **Figure 7**. Values are derived from AMSR2 brightness temperature data co-located to *Polarstern* (**Figure 4**).

3.4.2. Model experiment floe: Simulation of a glaze ice layer

Visual observations during the expedition and also the TLS reflectance data (Text S2, Figures S1 and S2) suggest the development of a glaze ice layer, which formed in some spots of the ice floe during the first warming event, and almost everywhere during the second one. Glaze ice layers at the top of the snowpack can have a strong impact on the microwave emission of the snow (Mätzler et al., 1984; Smith, 1996; Grenfell and Putkonen, 2008; Rees et al., 2010). Studies on the effect of such ice layers at the surface of the

snowpack have shown that, close to the Brewster angle (AMSR2 has an incident angle of 55°), they usually have a minor impact on vertically polarized TB, but strongly influence horizontally polarized TB (Rees et al., 2010) due to the high dielectric contrast between the snow and the ice layer. Thus, algorithms utilizing polarization differences or ratios (e.g., ASI and NASA-Team) will be influenced by the presence of such layers. How strong a certain frequency is impacted depends generally on the thickness of the ice layer (Montpetit et al., 2013). When we include such an ice layer in the SMP-based modeling, the modeled data (bottom panels in

Figure 7 show relative changes (increase in PR(19) and PD(89)) that are qualitatively comparable to the ones observed from satellite (**Figure 8**). GR(37/19) is hardly affected because it is based on vertically polarized TB, while PD at 37 GHz also shows a strong increase (not shown). As described in Text S3 and Text S4, several assumptions and simplifications had to be considered in the model setup. Therefore, we do not expect to match the satellite observations and do not analyze quantitative changes in detail. We believe that the strength of our modeling results lies in the qualitative understanding they provide of what has caused the observed changes in the satellite observations.

3.5. Site perspective: Ground-based radiometers

We next adopted the site perspective and investigated the ground-based radiometer measurements.

3.5.1. Brightness temperatures from ground-based radiometers

The TB of the ground-based radiometers between April 15 and April 21 are summarized in **Figure 9**. The analyzed period can be divided into four phases. The first phase is the period from April 15 to April 16 at noon, when the first warm air intrusion hit the MOSAiC site and the 2 m air temperatures are rising from -12°C to -2°C . Increased wind speed and (wet) snowfall led to changes in the snow cover. At, for example, 6.9 GHz horizontal polarization (**Figure 9b**), fluctuations during the peak of the first warm air intrusion indicate that surface properties in the FoV of the radiometer changed and that some low amount of liquid water might already have been building in the uppermost layer of the snowpack. However, these fluctuations can also be caused by snow dune

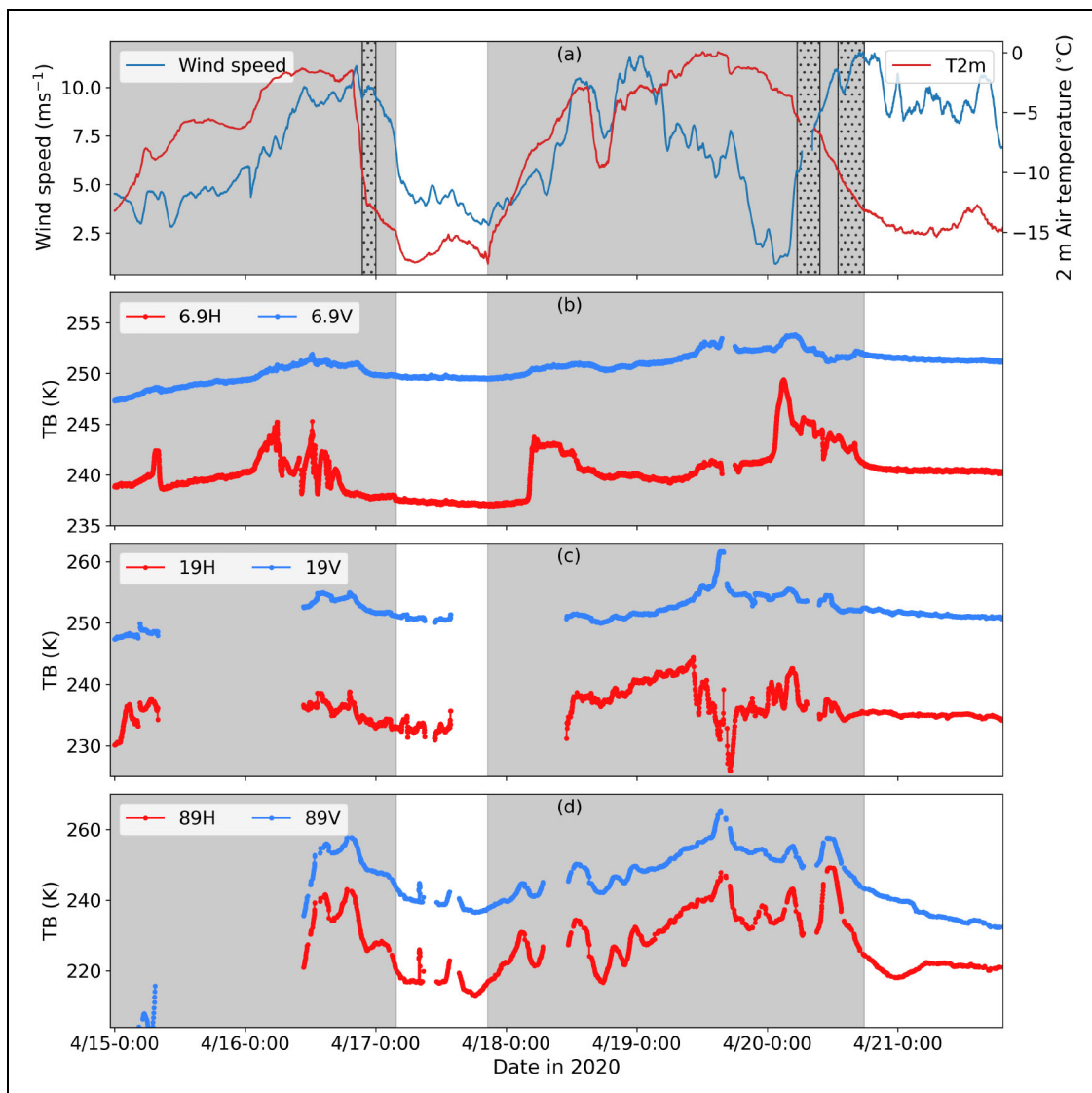


Figure 9. Meteorological conditions and brightness temperatures observed by the ground-based radiometers during the warming events. (a) 10 m wind speed and 2 m air temperature (T2 m) during the warm air intrusions. Three major snowfall events are also highlighted (stippled bars, **Figure 1**). (b)–(d) Observed brightness temperatures (TB) for vertical (V) and horizontal (H) polarizations for 6.9 GHz, 19 GHz, and 89 GHz, respectively. All data shown were smoothed, applying a running mean with a 1-hour window. Background shading indicates the four different phases for cloudy (gray) and clear sky (white) conditions. Dates are month/year-hour.

wandering through the FoV of the radiometer. At 19 GHz horizontal polarization, no such fluctuations are visible. Because these measurements were taken several meters apart from the 6.9 GHz observations, the snow conditions could have been very different during the first storm event. While the average brightness temperature at lower frequencies (6.9 to 19 GHz) increased only slightly, a strong increase can be found at 89 GHz (**Figure 9d**), indicating that mainly the temperature of the upper snow layer changed (89 GHz has the lowest penetration depth), which is consistent with **Figure 5**.

The second phase, between April 17 and April 18, is marked by a rapid cooling below -15°C , clear sky and calm conditions (**Figure 9**). TB at all frequencies were stable during this phase, with a slight cooling at 19 GHz and a strong drop in brightness temperature at 89 GHz.

The third phase marks the second, stronger warm air intrusion when the 2 m air temperature reached 0°C (**Figure 9**). Strong changes for horizontally polarized TB at all frequencies indicate changes in the snow surface due to snow fall and drift, as well as accumulation and possible formation of liquid water in the snow. However, during this period, increased snow accumulation around the instruments complicates the interpretation of the data at the remote sensing site, as the exact timings of snow dune formation are unknown.

Of special interest is the fourth phase, the period right after the second warming event, when a strong decline in TB is observed at higher frequencies (**Figure 9**). At 89 GHz, TB at both polarizations start decreasing around April 20 at 11:00. After 14:00 and until 18:00, TB at horizontal polarization decreased much faster than at vertical polarization, leading to an increase in polarization difference similar to what was observed from the satellites (**Figure 4**). We note that the start of this pronounced decrease coincides with a snowfall event, indicating that there could have been snow dune formations. However, in the case of snow drift through the FoV of the radiometer, we would expect higher temporal variability at horizontal polarization. Instead, TB decrease in an almost monotonic way.

At the lower frequencies, this drop in TB at horizontal polarization is less pronounced. In contrast to the satellite observations, the PD(89) of the ground-based observations recovers after less than 1 day and thus much faster than the satellite measurements. A likely explanation is the accumulation of snow in front of the ground-based radiometers, which is not recognizable on the satellite scale. These observations highlights the need for auxiliary data when using ground-based measurements to interpret satellite data due to the local snow conditions. Unlike the snow drifts that accumulated in front of the instruments, most of the level ice on the floe-scale did not experience accumulation during this event.

3.5.2. Model experiment on-ice site: Simulation of a glaze ice layer

Similar to the simulations of the SMP profiles (Section 3.4.2), we performed an experiment simulating the effect of a glaze ice layer in the FoV of the radiometers. In the

model, the glaze ice layer is approximated by a thin, radiometrically flat ice layer (≤ 1.6 mm) at top of the snowpack. The setup was chosen such that the model can reproduce the observed PD changes from the ground-based radiometer at 6.9 GHz and 89 GHz during phase 4, that is, the clear sky phase after the second warm air intrusion (fourth phase in **Figure 9**). As discussed earlier, during this phase, the increase in PD at 89 GHz cannot be explained by cloud forcing and is most likely due to the formation of a glaze ice layer in the FoV of the radiometer.

For the experiment we simulated an ice layer that starts developing on April 20 at around 14:00 and grows to 1.6 mm until 20:00. We then allowed layer of new snow to accumulate on top of this ice layer in order to reproduce the decrease in PD(89) from April 21 at 03:00 onward. We know of the increased snow accumulation in front of the instruments due to snow drift formation, as wind speed was high during this period (**Figure 9**); however, the exact timing of new snow accumulation remains unknown. The reflectance data from the TLS scan on April 22 show that a glaze ice layer was no longer visible in the FoV of the radiometers by this date. **Figure 10** shows the observed and simulated TB between April 20 at 14:00 and April 21 at 08:00. It is possible to reproduce the observed increase of polarization difference at 89 GHz with this setup, indicating that indeed the formation of a glaze ice layer likely explains the strong increase in observed PD89.

In summary, the temporal development of microwave TB measured by the on-ice radiometers and especially their polarization difference can be explained if a thin glaze ice layer is added in the microwave emission model. Such a glaze layer actually was observed in the field. In the model the effect of the glaze ice layer is larger at higher frequencies and mainly affects the polarization difference.

4. Discussion

The effects of the warm air intrusions on SIC retrievals are manifold, but we believe that we have identified dominant mechanisms for the case study presented here. First, the changed temperature gradients in the snow and snow metamorphism (increase in correlation length) influence SIC estimates that rely on the gradient ratio GR(37/19). While the polarization ratio is considered largely independent of physical temperature (Cavalieri et al., 1984; Comiso et al., 1997; Tonboe et al., 2006), such independence is not necessarily the case for the gradient ratio due to different penetration depths (and temperature-dependent permittivities) at 18.7 GHz and 36.5 GHz. Comiso et al. (1997) argued that the effect should be small unless the snow cover emits a sizable fraction of the measured TB. We assume the latter to be the case for 36.5 GHz. Thus we attribute the increase in GR(37/19) to the changed snow temperature (gradient) which is not fully compensated by snow metamorphism, that is, grain coarsening, which decreases GR(37/19). GR(37/19) can also be influenced by changes in snow height (due to increased scattering at 36.5 GHz), but observations from buoys deployed around the MOSAiC floe show that the (average) snow depth only changed by less than 5 cm during the investigated period (not shown).

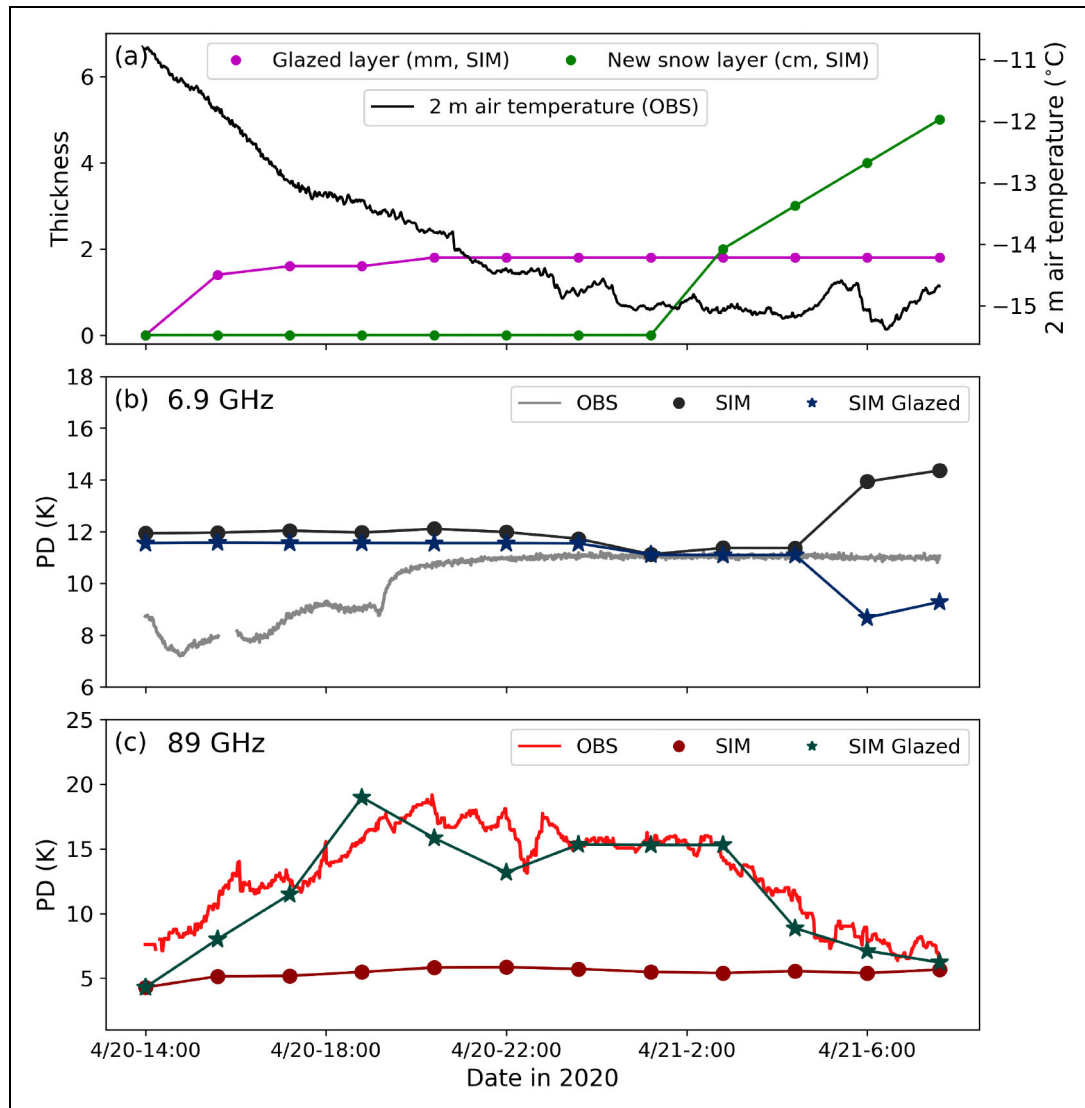


Figure 10. Model experiment adding a glaze ice layer on top of the snowpack. The model experiment covers a portion of phase 4 after the second warm air intrusion (Figure 9). Shown are (a) the thicknesses of the glaze ice layer (mm) and the snow layer (cm) used for the simulations, along with the observed 2 m air temperature; and the observed (OBS) and simulated (SIM) brightness temperatures for (b) polarization difference at 6.9 GHz, PD6.9, and (c) at 89 GHz, PD89, in simulations with the glaze layer included in the model setup (SIM Glazed) and without (SIM).

Second, we attribute the strong increase of satellite-measured PD after the warm air events to a glaze ice layer on top of the snow surface that was present on a large scale. Such glazing was observed in the field, and model results suggest that it can explain the observed satellite microwave TB. The alteration of TB because of the glazing causes a decrease in SIC in some SIC products that we investigated in this study, significantly for the algorithms that mainly rely on PD(89), as ASI does, or on PR(19) as NASA Team does. We hypothesize that the increase in PD at 36.5 GHz also caused the decrease in SIC by the OSI SAF algorithm that uses the TB space spanned by both polarizations at 36.5 GHz. The dual algorithm approach of the NSIDC CDR largely mitigates the glazing impact in this case, as the Bootstrap algorithm gives a high value for SIC. This algorithm is also based on both polarizations at 36.5 GHz but no decrease in SIC is observed after the warming events. A possible explanation here is an overestimation

and subsequent truncation of SIC to 100%. While this effect is an advantage for the case presented here, this approach might also overestimate SIC in other situations. For example, the Northeast Water polynya that opened at the Greenland coast after the events (middle column, first three rows in Figure 2) is hardly visible in the NSIDC CDR product.

We note a stronger response of the microwave emissions to the warming events at higher frequencies that have smaller penetration depths into the snow than at lower frequencies. A thin ice crust also has a greater effect at these frequencies while the wavelengths of the lower frequencies are large compared to the thickness of the crust. SIC retrievals using vertical polarization or ones that are based on lower frequencies like 6.9 GHz are less affected.

Hypothesizing that such glazing events should increase in a warming Arctic, as not only warm air intrusions but

also rain on snow events can cause them (Stroeve et al., 2022), we find that algorithms based on low frequencies vertical polarization could be a more robust choice for the future. In the study by Rees et al. (2010) about an ice crust on snow on land 6.9 GHz also showed the least response to the ice crust. As a difference to our case, PD at 19 GHz was affected most in their study, which is likely due to a different thickness of the ice crust and different snow conditions.

Modeling snow and ice microwave emission remains a challenge especially at satellite-footprint scale, even if a large amount of observational data is available. The challenge is partly due to the local heterogeneity which makes matching radiometer observations and ground-based observations difficult. For example, we did not only observe differences in the snow cover between the ground-based radiometer footprints at the same site but also within one footprint (Figure S3). We overcame this problem by using the vast amount of snow profiles from the SMP measurements in combination with modeling, providing a statistical description of expected surface TB (Figure 7). If, however, the radiometers measure snow conditions that are not representative of the surroundings (due to snow accumulation), then comparisons to these TB measurements are impeded. The statistical description might be more comparable to a satellite observation in the case of negligible atmospheric effects. We cannot be certain, however, that the SMP data are representative of a satellite footprint on the order of tens of kilometres. Also, certain parameters, such as surface roughness that are important for emission modeling of satellite observations, were not directly available. Coherence effects, that depend on frequency and layer thickness, are another source of uncertainty. Nevertheless, the temporal evolution of the ground-based radiometer measurements can be reproduced by a microwave emission model if the glaze ice layer is included. Similarly, including a glaze layer allowed us to qualitatively model relative changes as observed from space using the SMP measurements as input. This study is one of the few existing cases where a spurious change in satellite SIC can be fully explained by the observed surface changes from ground-based measurements (snow and ice physics and radiometers). We are confident that adopting the three perspectives from the different scales (satellite, floe, site) allowed for a plausible interpretation of the observations.

5. Conclusion

Arctic amplification, that is, the more rapid and stronger increase of temperatures in the Arctic compared to low latitudes (Screen and Simmonds, 2010; Serreze and Barry, 2011; Comiso and Hall, 2014; Wendisch et al., 2017; Wendisch et al., 2023) can lead to an increased occurrence of warm air intrusions above the ice cover (Graham et al., 2017). As shown in this study, they can affect TB measured by satellite microwave radiometers and cause uncertainties and errors in the derived SIC products. In our case, the warm air intrusions led to a large-scale spurious strong decrease in SIC and an increase in the deviations between different SIC products in the central Arctic. These

deviations lasted for several days. Only one product was minimally affected. It, however, has the tendency to always produce high SIC values, which was the correct solution in this case.

Here we have offered an interpretation of the satellite signals based on observations from the MOSAiC expedition and by microwave emission modeling, taking into account atmospheric effects as well as surface snow metamorphism. As an explanation for the changed microwave emissions during and after the warming events, we propose the formation of a large-scale glaze ice layer, which persists even days after the warm air intrusion.

Many recent SIC studies (Lu et al., 2022) focus on how the atmosphere influences TB and thus SIC retrievals. In our case, the surface changes are highly relevant and should be included in future evaluations of SIC retrieval algorithms. Ivanova et al. (2015) conjectured that near 90 GHz algorithms might be less sensitive to changes within the snow compared to the lower frequencies because of the small penetration depth. However, as shown in this study, certain surface effects like glazing can have a strong influence on these algorithms. Identifying similar events, their scale in time and space and their frequencies of occurrence can provide additional insights to quantify whether this effect is significant on longer temporal and spatial scales and for climate data records. Inter-comparison studies of SIC algorithms could also benefit from an evaluation of the performance of the algorithm during events like warm air intrusions or rain-on-snow events, which can lead to the formation of a glaze ice layer. In the future, due to a projected increase in warm air intrusions, the relevance of their effects on sea ice climate records from satellites and the distinction between actual influence of climate warming on sea ice, as described for example by Merkouriadi et al. (2020), and retrieval uncertainties will become more important. The effects of warm air intrusions need to be considered in the estimation of product uncertainties, possibly by using dynamic uncertainty estimates, that is, uncertainties that are neither constant nor dependent only on SIC. An example is the OSI SAF iCDR product which provides estimates that show an increased uncertainty after the events, even though the higher uncertainty is caused, in this case, by a higher representativeness uncertainty.

Multi-frequency methods exploiting the synergy of the robustness of 6.9 GHz and the high spatial resolution of 89 GHz are a promising approach for future retrievals. Upcoming satellite missions like the Copernicus Imaging Microwave Radiometer (Donlon, 2020) will provide measurements at 6.9 GHz at a much higher spatial resolution (around 15 km) than current satellite sensors, which makes it well suited for SIC retrievals at higher spatial resolution (5 km at 37 GHz) and higher accuracy (using 6.9 GHz) than what is available today.

Data accessibility statement

The AMSR2 satellite data are available via Japan Aerospace Exploration Agency's G-Portal <https://gportal.jaxa.jp/gpr/?lang=en>. The NOAA/NSIDC Climate Data Record of Passive Microwave Sea Ice Concentration, Version 4 is

available via <https://nsidc.org/data/g02202/versions/4>. The OSI 430-b SIC product data are available via <https://osi-saf.eumetsat.int/> (copyright 2021 EUMETSAT). The radiometer, snow, temperature, laser scan, and radio-sonde data used in this manuscript were produced as part of the international Multidisciplinary drifting Observatory for the Study of the Arctic Climate (MOSAiC) with the tag MOSAiC20192020 and the Project ID: AWI PS122 00. The HUTRAD radiometer data are available via PANGAEA, <https://doi.org/10.1594/PANGAEA.954608>. The radio-sonde data are available via PANGAEA, <https://doi.org/10.1594/PANGAEA.928656>. The HATPRO LWP data product are available via PANGAEA, <https://doi.org/10.1594/PANGAEA.941389>. The near-surface temperature measurements are available from the Arctic Data Center (Cox et al., 2021). The Present Weather Detector 22 precipitation gauge data is accessible via ARM: https://adc.arm.gov/discovery/#/results/instrument_code::pwd, last access: November 7, 2022. The SBR radiometer data are available via PANGAEA, <https://doi.pangaea.de/10.1594/PANGAEA.956108>. The TLS data are available via the Arctic Data Center (Clemens-Sewall, 2021). ERA5 data are made available by the Copernicus Climate Change Service (C3S) at <https://cds.climate.copernicus.eu/cdsapp#!/home>. C3S (2017): ERA5. Fifth generation of European Centre for Medium-range Weather Forecasts atmospheric reanalyses of the global climate. Copernicus Climate Change Service Climate Data Store, 2017–2020.

Supplemental files

The supplemental files for this article can be found as follows:

Supplement.pdf.

Acknowledgments

This work was carried out, and data used in this manuscript was produced, as part of the international Multidisciplinary drifting Observatory for the Study of the Arctic Climate (MOSAiC) with the tag MOSAiC20192020. The authors thank all persons involved in the expedition of the research vessel *Polarstern* during MOSAiC in 2019–2020 (AWI_PS122_00) as listed in Nixdorf et al. (2021). Additionally the authors would like to thank Robert Hausen and Linda Thielke for information and discussions, Matthew Shupe for support with the meteorological tower measurements, Ronny Engelmann and the TROPOS institute for acquiring the HATPRO measurements onboard, Tânia Casal, Craig Donlon from ESA, and Roger Jové Casulleras from Balamis for supporting HUTRAD for MOSAiC, and Eric Brossier and Calle Schönning for their assistance with TLS measurements.

Funding

The authors gratefully acknowledge the funding by the Deutsche Forschungsgemeinschaft (DFG, German Research Foundation) through the Transregional Collaborative Research Centre TRR-172 “Arctic Amplification: Climate Relevant Atmospheric and Surface Processes, and Feedback Mechanisms (AC³)” (grant 268020496) and the MOSAiCmicrowaveRS project (grant 420499875). Further

funding was provided by the Bundesministerium für Bildung und Forschung (BMBF) through the IceSense project (grant BMBF 03F0866B). The microwave radiometer HUTRAD measurements were funded by ESA through the CIMRex (contract 4000125503/18/NL/FF/gp) project; the HATPRO radiometer by BMBF under FKZ: 01LKL1603A. D.C.S. was supported by NSF OPP-1724540.

Competing interests

The authors have declared that no competing interests exist.

Author contributions

Contributed equally to this work: JER, PR.

First description and interpretation of event: LK.

Conception and design of this study: JER, PR, MH, GS.

Acquisition of data: MH, GS, LK, ARM, RN, JS.

Analysis and interpretation of data: JER, PR, MH, DCS, KE, LK, JL, ARM, AW, GS.

Drafting, and revising this article: All authors.

Approval of the version to be submitted: All authors.

References

- Andersen, S, Tonboe, R, Kaleschke, L, Heygster, G, Pedersen, LT.** 2007. Intercomparison of passive microwave sea ice concentration retrievals over the high-concentration Arctic sea ice. *Journal of Geophysical Research: Oceans* **112**(C8). DOI: <http://dx.doi.org/10.1029/2006JC003543>.
- Andersen, S, Tonboe, R, Kern, S, Schyberg, H.** 2006. Improved retrieval of sea ice total concentration from spaceborne passive microwave observations using numerical weather prediction model fields: An intercomparison of nine algorithms. *Remote Sensing of Environment* **104**(4): 374–392. DOI: <http://dx.doi.org/10.1016/j.rse.2006.05.013>.
- Aue, L, Vihma, T, Uotila, P, Rinke, A.** 2022. New insights into cyclone impacts on sea ice in the Atlantic sector of the Arctic Ocean in winter. *Geophysical Research Letters* **49**(22): e2022GL100051. DOI: <http://dx.doi.org/10.1029/2022GL100051>.
- Bartelt, P, Lehning, M.** 2002. A physical SNOWPACK model for the swiss avalanche warning: Part I: Numerical model. *Cold Regions Science and Technology* **35**: 123–145. DOI: [http://dx.doi.org/10.1016/S0165-232X\(02\)00074-5](http://dx.doi.org/10.1016/S0165-232X(02)00074-5).
- Cavalieri, DJ, Gloersen, P, Campbell, WJ.** 1984. Determination of sea ice parameters with the NIMBUS 7 SMMR. *Journal of Geophysical Research: Atmospheres* **89**: 5355–5369. DOI: <http://dx.doi.org/10.1029/JD089iD04p05355>.
- Cavalieri, DJ, Parkinson, CL, Gloersen, P, Zwally, HJ.** 1997. Arctic and Antarctic sea ice concentrations from multichannel passive-microwave satellite data sets: October 1978–September 1995 user's guide. NASA Goddard Space Flight Center. Available at <https://ntrs.nasa.gov/citations/19980076134>. Accessed September 16, 2022.
- Clemens-Sewall, D.** 2021. Terrestrial laser scans of the on-ice remote sensing instrument site on the

- Multidisciplinary Drifting Observatory for the Study of Arctic Climate (MOSAiC) in April 2020 (Leg 3). Arctic Data Center. DOI: <http://dx.doi.org/10.18739/A25717P9Q>.
- Clemens-Sewall, D, Parno, M, Perovich, D, Polashenski, C, Raphael, IA.** 2022a. FlakeOut: A geometric approach to remove wind-blown snow from terrestrial laser scans. *Cold Regions Science and Technology* **201**: 103611. DOI: <http://dx.doi.org/10.1016/j.coldregions.2022.103611>.
- Clemens-Sewall, D, Polashenski, C, Frey, MM, Cox, CJ, Granskog, MA, Macfarlane, AR, Fons, SW, Schmale, J, Hutchings, JK, von Albedyll, L, Arndt, S, Schneebeli, M, Perovich, D.** 2023. Snow loss into leads in Arctic sea ice: Minimal in typical wintertime conditions, but high during a warm and windy snowfall event. *Geophysical Research Letters* **50**(12): e2023GL102816. DOI: <http://dx.doi.org/10.1029/2023GL102816>.
- Clemens-Sewall, D, Polashenski, C, Raphael, I, Perovich, D, Fons, S, Itkin, P, Jaggi, M, Jutila, A, Macfarlane, A, Matero, I, Oggier, M, Wagner, D, Visser, R, Olufson, T, Radenz, M, Schönning, C, Hansen, J, Votvik, M, Brossier, E, Svavarsdottir, S.** 2022b. High-resolution repeat topography of drifting ice floes in the Arctic Ocean from terrestrial laser scanning collected on the Multidisciplinary Drifting Observatory for the Study of Arctic Climate Expedition. NSF Arctic Data Center. DOI: <http://dx.doi.org/10.18739/A26688K9D>.
- Comiso, JC.** 1986. Characteristics of Arctic winter sea ice from satellite multispectral microwave observations. *Journal of Geophysical Research: Oceans* **91**(C1): 975–994. DOI: <http://dx.doi.org/10.1029/JC091iC01p00975>.
- Comiso, JC, Cavalieri, DJ, Parkinson, CL, Gloersen, P.** 1997. Passive microwave algorithms for sea ice concentration: A comparison of two techniques. *Remote Sensing of Environment* **60**(3): 357–384. DOI: [http://dx.doi.org/10.1016/S0034-4257\(96\)00220-9](http://dx.doi.org/10.1016/S0034-4257(96)00220-9).
- Comiso, JC, Gersten, RA, Stock, LV, Turner, J, Perez, GJ, Cho, K.** 2017. Positive trend in the Antarctic sea ice cover and associated changes in surface temperature. *Journal of Climate* **30**(6): 2251–2267. DOI: <http://dx.doi.org/10.1175/JCLI-D-16-0408.1>.
- Comiso, JC, Hall, DK.** 2014. Climate trends in the Arctic as observed from space. *WIREs Climate Change* **5**(3): 389–409. DOI: <http://dx.doi.org/10.1002/wcc.277>.
- Cox, C, Gallagher, M, Shupe, M, Persson, O, Solomon, A, Blomquist, B, Brooks, I, Costa, D, Gottas, D, Hutchings, J, Osborn, J, Morris, S, Preusser, A, Uttal, T.** 2021. 10-meter (m) meteorological flux tower measurements (Level 1 Raw), Multidisciplinary Drifting Observatory for the Study of Arctic Climate (MOSAiC), central Arctic, October 2019–September 2020. Arctic Data Center. DOI: <http://dx.doi.org/10.18739/A2VM42Z5F>.
- Dada, L, Angot, H, Beck, I, Baccarini, A, Quéléver, LLJ, Boyer, M, Laurila, T, Brasseur, Z, Jozef, G, de Boer, G, Shupe, MD, Henning, S, Bucci, S, Dütsch, M, Stohl, A, Petäjä, T, Daellenbach, KR, Jokinen, T, Schmale, J.** 2022. A central Arctic extreme aerosol event triggered by a warm air-mass intrusion. *Nature Communications* **13**: 5290. DOI: <http://dx.doi.org/10.1038/s41467-022-32872-2>.
- Deems, JS, Painter, TH, Finnegan, DC.** 2013. Lidar measurement of snow depth: A review. *Journal of Glaciology* **59**(215): 467–479. DOI: <http://dx.doi.org/10.3189/2013JoG12J154>.
- Donlon, C.** 2020. Copernicus imaging microwave radiometer (CIMR) mission requirements document. Noordwijk, The Netherlands: European Space Agency: Issue number 4, Version 4.0.
- EUMETSAT Ocean and Sea Ice Satellite Application Facility.** 2017. Global sea ice concentration interim climate data record 2016-onwards (v2.0, 2017), OSI-430-b. EUMETSAT Ocean and Sea Ice Satellite Application Facility (Data extracted from OSI SAF FTP server/EUMETSAT Data Center: April 2020, Northern Hemisphere). Accessed September 7, 2021.
- Fox-Kemper, B, Hewitt, H, Xiao, C, Aðalgeirsdóttir, G, Drijfhout, S, Edwards, T, Golledge, N, Hemer, M, Kopp, R, Krinner, G, Mix, A, Notz, D, Nowicki, S, Nurhati, I, Ruiz, L, Sallée, JB, Slangen, A, Yu, Y.** 2021. Ocean, cryosphere and sea level change, in Masson-Delmotte, V, Zhai, P, Pirani, A, Connors, S, Péan, C, Berger, S, Caud, N, Chen, Y, Goldfarb, L, Gomis, M, Huang, M, Leitzell, K, Lonnoy, E, Matthews, J, Maycock, T, Waterfield, T, Yelekçi, O, Yu, R, Zhou, B eds., *Climate change 2021: The physical science basis. Contribution of Working Group I to the Sixth Assessment Report of the Intergovernmental Panel on Climate Change*. Cambridge, UK: Cambridge University Press: 1211–1362. DOI: <http://dx.doi.org/10.1017/9781009157896.011>.
- Graham, RM, Cohen, L, Petty, AA, Boisvert, LN, Rinke, A, Hudson, SR, Nicolaus, M, Granskog, MA.** 2017. Increasing frequency and duration of Arctic winter warming events. *Geophysical Research Letters* **44**(13): 6974–6983. DOI: <http://dx.doi.org/10.1002/2017GL073395>.
- Grenfell, TC, Putkonen, J.** 2008. A method for the detection of the severe rain-on-snow event on Banks Island, October 2003, using passive microwave remote sensing. *Water Resources Research* **44**(3): W03425. DOI: <http://dx.doi.org/10.1029/2007WR005929>.
- Hao, M, Luo, Y, Lin, Y, Zhao, Z, Wang, L, Huang, J.** 2019. Contribution of atmospheric moisture transport to winter Arctic warming. *International Journal of Climatology* **39**(5): 2697–2710. DOI: <http://dx.doi.org/10.1002/joc.5982>.
- Henderson, GR, Barrett, BS, Wachowicz, LJ, Mattingly, KS, Preece, JR, Mote, TL.** 2021. Local and remote atmospheric circulation drivers of Arctic change: A review. *Frontiers in Earth Science* **9**: 549. DOI: <http://dx.doi.org/10.3389/feart.2021.709896>.
- Hersbach, H, Bell, B, Berrisford, P, Hirahara, S, Horányi, A, Muñoz-Sabater, J, Nicolas, J, Peubey, C,**

- Radu, R, Schepers, D, Simmons, A, Soci, C, Abdalla, S, Abellan, X, Balsamo, G, Bechtold, P, Biavati, G, Bidlot, J, Bonavita, M, Chiara, GD, Dahlgren, P, Dee, D, Diamantakis, M, Dragani, R, Flemming, J, Forbes, R, Fuentes, M, Geer, A, Haimberger, L, Healy, S, Hogan, RJ, Hólm, E, Janisková, M, Keeley, S, Laloyaux, P, Lopez, P, Lupu, C, Radnoti, G, Rosnay, Pd, Rozum, I, Vamborg, F, Villaume, S, Thépaut, JN.** 2020. The ERA5 global reanalysis. *Quarterly Journal of the Royal Meteorological Society* **146**(730): 1999–2049. DOI: <http://dx.doi.org/10.1002/qj.3803>.
- Hwang, BJ, Ehn, JK, Barber, DG, Galley, R, Grenfell, TC.** 2007. Investigations of newly formed sea ice in the Cape Bathurst polynya: 2. Microwave emission. *Journal of Geophysical Research: Oceans* **112**(C5). DOI: <http://dx.doi.org/10.1029/2006JC003703>.
- Hyland, RW, Wexler, A.** 1983. Formulations for the thermodynamic properties of the saturated phases of H₂O from 173.15 K to 473.15 K. *Ashrae Transactions* **89**: 500–520.
- Ivanova, N, Pedersen, LT, Tonboe, RT, Kern, S, Heygster, G, Lavergne, T, Sørensen, A, Saldo, R, Dybkjær, G, Brucker, L, Shokr, M.** 2015. Inter-comparison and evaluation of sea ice algorithms: Towards further identification of challenges and optimal approach using passive microwave observations. *The Cryosphere* **9**(5): 1797–1817. DOI: <http://dx.doi.org/10.5194/tc-9-1797-2015>.
- Kaleschke, L, Lüpkes, C, Vihma, T, Haarpaintner, J, Bochert, A, Hartmann, J, Heygster, G.** 2001. SSM/I sea ice remote sensing for mesoscale ocean-atmosphere interaction analysis. *Canadian Journal of Remote Sensing* **27**(5): 526–537. DOI: <http://dx.doi.org/10.1080/07038992.2001.10854892>.
- Kern, S, Lavergne, T, Notz, D, Pedersen, LT, Tonboe, RT, Saldo, R, Sørensen, AM.** 2019. Satellite passive microwave sea-ice concentration data set intercomparison: Closed ice and ship-based observations. *The Cryosphere* **13**(12): 3261–3307. DOI: <http://dx.doi.org/10.5194/tc-13-3261-2019>.
- Kern, S, Lavergne, T, Pedersen, LT, Tonboe, RT, Bell, L, Meyer, M, Zeigermann, L.** 2022. Satellite passive microwave sea-ice concentration data set intercomparison using Landsat data. *The Cryosphere* **16**(1): 349–378. DOI: <http://dx.doi.org/10.5194/tc-16-349-2022>.
- King, J, Howell, S, Brady, M, Toose, P, Derksen, C, Haas, C, Beckers, J.** 2020. Local-scale variability of snow density on Arctic sea ice. *The Cryosphere* **14**(12): 4323–4339. DOI: <http://dx.doi.org/10.5194/tc-14-4323-2020>.
- Knust, R.** 2017. Polar research and supply vessel POLARSTERN operated by the Alfred-Wegener-Institute. *Journal of Large-Scale Research Facilities* **3**(A119). DOI: <http://dx.doi.org/10.17815/jlsrf-3-163>.
- Lavergne, T, Sørensen, AM, Kern, S, Tonboe, R, Notz, D, Aaboe, S, Bell, L, Dybkjær, G, Eastwood, S, Gabarro, C, Heygster, G, Killie, MA, Brandt Kreiner, M, Lavelle, J, Saldo, R, Sandven, S, Pedersen, LT.** 2019. Version 2 of the EUMETSAT OSI SAF and ESA CCI sea-ice concentration climate data records. *The Cryosphere* **13**(1): 49–78. DOI: <http://dx.doi.org/10.5194/tc-13-49-2019>.
- Lehning, M, Bartelt, P, Brown, B, Fierz, C.** 2002a. A physical SNOWPACK model for the Swiss avalanche warning: Part III: Meteorological forcing, thin layer formation and evaluation. *Cold Regions Science and Technology* **35**: 169–184. DOI: [http://dx.doi.org/10.1016/S0165-232X\(02\)00072-1](http://dx.doi.org/10.1016/S0165-232X(02)00072-1).
- Lehning, M, Bartelt, P, Brown, B, Fierz, C, Satyawali, P.** 2002b. A physical SNOWPACK model for the Swiss avalanche warning: Part II: Snow microstructure. *Cold Regions Science and Technology* **35**: 147–167. DOI: [http://dx.doi.org/10.1016/S0165-232X\(02\)00073-3](http://dx.doi.org/10.1016/S0165-232X(02)00073-3).
- Liu, G, Curry, JA.** 2003. Observation and interpretation of microwave cloud signatures over the Arctic Ocean during winter. *Journal of Applied Meteorology* **42**: 51–64. DOI: [http://dx.doi.org/10.1175/1520-0450\(2003\)042<0051:OAIOMC>2.0.CO;2](http://dx.doi.org/10.1175/1520-0450(2003)042<0051:OAIOMC>2.0.CO;2).
- Lu, J, Scarlat, R, Heygster, G, Spreen, G.** 2022. Reducing weather influences on an 89 GHz sea ice concentration algorithm in the Arctic using retrievals from an optimal estimation method. *Journal of Geophysical Research: Oceans* **127**(9): e2019JC015912. DOI: <http://dx.doi.org/10.1029/2019JC015912>.
- Macfarlane, AR, Schneebeli, M, Dadic, R, Wagner, DN, Arndt, S, Clemens-Sewall, D, Hämmerle, S, Hannula, HR, Jaggi, M, Kolabutin, N, Krampe, D, Lehning, M, Matero, I, Nicolaus, M, Oggier, M, Pirazzini, R, Polashenski, C, Raphael, I, Regnery, J, Shimanchuck, E, Smith, MM, Tavri, A.** 2021. Snowpit SnowMicroPen (SMP) force profiles collected during the MOSAiC expedition. PANGAEA. DOI: <http://dx.doi.org/10.1594/PANGAEA.935554>.
- Maeda, T, Taniguchi, Y, Imaoka, K.** 2016. GCOM-W1 AMSR2 Level 1R product: Dataset of brightness temperature modified using the antenna pattern matching technique. *IEEE Transactions on Geoscience and Remote Sensing* **54**(2): 770–782. DOI: <http://dx.doi.org/10.1109/TGRS.2015.2465170>.
- Maturilli, M, Holdridge, DJ, Dahlke, S, Graeser, J, Sommerfeld, A, Jaiser, R, Deckelmann, H, Schulz, A.** 2021. Initial radiosonde data from 2019-10 to 2020-09 during project MOSAiC [dataset]. Alfred Wegener Institute, Helmholtz Centre for Polar and Marine Research, Bremerhaven, Germany. PANGAEA. DOI: <http://dx.doi.org/10.1594/PANGAEA.928656>. Accessed March 30, 2021.
- Mätzler, C, Ramseier, R, Svendsen, E.** 1984. Polarization effects in seaice signatures. *IEEE Journal of Oceanic Engineering* **9**(5): 333–338. DOI: <http://dx.doi.org/10.1109/JOE.1984.1145646>.
- Meier, WN, Fetterer, F, Windnagel, AK, Stewart, S.** 2021. NOAA/NSIDC climate data record of passive microwave sea ice concentration, Version 4 [dataset]. Boulder, CO: NSIDC, National Snow and Ice Data Center. DOI: <http://dx.doi.org/10.7265/efmz-2t65>. Accessed September 18, 2022.

- Meier, WN, Stroeve, JC.** 2022. An updated assessment of the changing Arctic sea ice cover. *Oceanography* **35**(3–4): 10–19. DOI: <http://dx.doi.org/10.5670/oceanog.2022.114>.
- Melsheimer, C.** 2019. ASI version 5 sea ice concentration user guide (Version 0.9.2). Bremen, Germany: Institute of Environmental Physics, University of Bremen.
- Meredith, M, Sommerkorn, M, Cassotta, S, Derksen, C, Ekaykin, A, Hollowed, A, Kofinas, G, Mackintosh, A, Melbourne-Thomas, J, Muelbert, M, Ottersen, G, Pritchard, H, Schuur, E.** 2019. 2019: Polar regions, in Pörtner, HO, Roberts, D, Masson-Delmotte, V, Zhai, P, Tignor, M, Poloczanska, E, Mintenbeck, K, Alegra, A, Nicolai, M, Okem, A, Petzold, J, Rama, B, Weyer, N eds., *IPCC special report on the ocean and cryosphere in a changing climate*. Cambridge, UK: Cambridge University Press.
- Merkouriadi, I, Cheng, B, Hudson, S, Granskog, M.** 2020. Effect of frequent winter warming events (storms) and snow on sea-ice growth—A case from the Atlantic sector of the Arctic Ocean during the N-ICE2015 campaign. *Annals of Glaciology* **61**: 1–7. DOI: <http://dx.doi.org/10.1017/aog.2020.25>.
- Montpetit, B, Royer, A, Roy, A, Langlois, A, Derksen, C.** 2013. Snow microwave emission modeling of ice lenses within a snowpack using the microwave emission model for layered snowpacks. *IEEE Transactions on Geoscience and Remote Sensing* **51**(9): 4705–4717. DOI: <http://dx.doi.org/10.1109/TGRS.2013.2250509>.
- Nicolaus, M, Jutila, A, Raphael, I, Hoppman, M.** 2021. Snow height on sea ice, meteorological conditions and drift of sea ice from autonomous measurements from buoy 2020S99, deployed during MOSAiC 2019/20. Alfred Wegener Institute, Helmholtz Centre for Polar and Marine Research, Bremerhaven, Germany. PANGAEA. DOI: <http://dx.doi.org/10.1594/PANGAEA.936227>.
- Nicolaus, M, Perovich, DK, Spreen, G, Granskog, MA, von Albedyll, L, Angelopoulos, M, Anhaus, P, Arndt, S, Belter, HJ, Bessonov, V, Birnbaum, G, Brauchle, J, Calmer, R, Cardellach, E, Cheng, B, Clemens-Sewall, D, Dadic, R, Damm, E, de Boer, G, Demir, O, Dethloff, K, Divine, DV, Fong, AA, Fons, S, Frey, MM, Fuchs, N, Gabarró, C, Gerland, S, Goessling, HF, Gradinger, R, Haapala, J, Haas, C, Hamilton, J, Hannula, HR, Hendricks, S, Herber, A, Heuzé, C, Hoppmann, M, Høyland, KV, Huntemann, M, Hutchings, JK, Hwang, B, Itkin, P, Jacobi, HW, Jaggi, M, Jutila, A, Kaleschke, L, Katlein, C, Kolabutin, N, Krampe, D, Kristensen, SS, Krumpfen, T, Kurtz, N, Lampert, A, Lange, BA, Lei, R, Light, B, Linhardt, F, Liston, GE, Loose, B, Macfarlane, AR, Mahmud, M, Matero, IO, Maus, S, Morgenstern, A, Naderpour, R, Nandan, V, Niubom, A, Oggier, M, Oppelt, N, Pätzold, F, Perron, C, Petrovsky, T, Pirazzini, R, Polashenski, C, Rabe, B, Raphael, IA, Regnery, J, Rex, M, Ricker, R, Riemann-Campe, K, Rinke, A, Rohde, J, Salganik, E, Scharien, RK, Schiller, M, Schneebeli, M, Semmling, M, Shimanchuk, E, Shupe, MD, Smith, MM, Smolyanitsky, V, Sokolov, V, Stanton, T, Stroeve, J, Thielke, L, Timofeeva, A, Tonboe, RT, Tavri, A, Tsamados, M, Wagner, DN, Watkins, D, Webster, M, Wendisch, M.** 2022. Overview of the MOSAiC expedition: Snow and sea ice. *Elementa: Science of the Anthropocene* **10**(1). DOI: <http://dx.doi.org/10.1525/elementa.2021.000046>.
- Nixdorf, U, Dethloff, K, Rex, M, Shupe, M, Sommerfeld, A, Perovich, DK, Nicolaus, M, Heuzé, C, Rabe, B, Loose, B, Damm, E, Gradinger, R, Fong, A, Maslowski, W, Rinke, A, Kwok, R, Spreen, G, Wendisch, M, Herber, A, Hirsekorn, M, Mohaupt, V, Frickenhaus, S, Immerz, A, Weiss-Tuider, K, König, B, Menedoht, D, Regnery, J, Gerchow, P, Ransby, D, Krumpfen, T, Morgenstern, A, Haas, C, Kanzow, T, Rack, FR, Saitzev, V, Sokolov, V, Makarov, A, Schwarze, S, Wunderlich, T, Wurr, K, Boetius, A.** 2021. MOSAiC extended acknowledgement. Zenodo. DOI: <http://dx.doi.org/10.5281/zenodo.5179739>.
- Nomokonova, T, Ebell, K, Löhnert, U, Maturilli, M, Ritter, C, O'Connor, E.** 2019. Statistics on clouds and their relation to thermodynamic conditions at Ny-Ålesund using ground-based sensor synergy. *Atmospheric Chemistry and Physics* **19**(6): 4105–4126. DOI: <http://dx.doi.org/10.5194/acp-19-4105-2019>.
- Oelke, C.** 1997. Atmospheric signatures in sea-ice concentration estimates from passive microwaves: Modelled and observed. *International Journal of Remote Sensing* **18**: 1113–1136. DOI: <http://dx.doi.org/10.1080/014311697218601>.
- Onstott, RG, Grenfell, TC, Matzler, C, Luther, CA, Svendsen, EA.** 1987. Evolution of microwave sea ice signatures during early summer and midsummer in the marginal ice zone. *Journal of Geophysical Research: Oceans* **92**(C7): 6825–6835. DOI: <http://dx.doi.org/10.1029/JC092iC07p06825>.
- Perovich, DK, Meier, TWM, Farrell, SL, Hendricks, S, Gerland, S, Haas, C, Krumpfen, T, Polashenski, C, Ricker, R, Webster, M.** 2017. Sea ice [in Arctic report card 2017]. Available at <http://www.arctic.noaa.gov/Report-Card>. Accessed September 17, 2022.
- Proksch, M, Löwe, H, Schneebeli, M.** 2015. Density, specific surface area, and correlation length of snow measured by high-resolution penetrometry. *Journal of Geophysical Research: Earth Surface* **120**(2): 346–362. DOI: <http://dx.doi.org/10.1002/2014JF003266>.
- Rabe, B, Heuzé, C, Regnery, J, Aksenov, Y, Allerholt, J, Athanase, M, Bai, Y, Basque, C, Bauch, D, Baumann, TM, Chen, D, Cole, ST, Craw, L, Davies, A, Damm, E, Dethloff, K, Divine, DV, Doglioni, F, Ebert, F, Fang, YC, Fer, I, Fong, AA, Gradinger, R, Granskog, MA, Graupner, R, Haas, C, He, H, He, Y, Hoppmann, M, Janout, M, Kadko, D, Kanzow, T, Karam, S, Kawaguchi, Y, Koenig, Z, Kong, B, Krishfield, RA, Krumpfen, T, Kuhlmeier, D, Kuznetsov, I, Lan, M, Laukert, G, Lei, R, Li, T, Torres-Valdés, S, Lin, L, Lin, L, Liu, H, Liu, N, Loose, B, Ma, X, McKay, R, Mallet, M, Mallett, RDC,**

- Maslowski, W, Mertens, C, Mohrholz, V, Muilwijk, M, Nicolaus, M, O'Brien, JK, Perovich, D, Ren, J, Rex, M, Ribeiro, N, Rinke, A, Schaffer, J, Schuffenhauer, I, Schulz, K, Shupe, MD, Shaw, W, Sokolov, V, Sommerfeld, A, Spreen, G, Stanton, T, Stephens, M, Su, J, Sukhikh, N, Sundfjord, A, Thomisch, K, Tippenhauer, S, Toole, JM, Vredenburg, M, Walter, M, Wang, H, Wang, L, Wang, Y, Wendisch, M, Zhao, J, Zhou, M, Zhu, J. 2022. Overview of the MOSAiC expedition: Physical oceanography. *Elementa: Science of the Anthropocene* **10**(1). DOI: <http://dx.doi.org/10.1525/elementa.2021.00062>.
- Rees, A, Lemmetyinen, J, Derksen, C, Pulliainen, J, English, M. 2010. Observed and modelled effects of ice lens formation on passive microwave brightness temperatures over snow covered tundra. *Remote Sensing of Environment* **114**(1): 116–126. DOI: <http://dx.doi.org/10.1016/j.rse.2009.08.013>.
- Rinke, A, Cassano, JJ, Cassano, EN, Jaiser, R, Handorf, D. 2021. Meteorological conditions during the MOSAiC expedition: Normal or anomalous? *Elementa: Science of the Anthropocene* **9**(1). DOI: <http://dx.doi.org/10.1525/elementa.2021.00023>.
- Rinke, A, Maturilli, M, Graham, RM, Matthes, H, Handorf, D, Cohen, L, Hudson, SR, Moore, JC. 2017. Extreme cyclone events in the Arctic: Wintertime variability and trends. *Environmental Research Letters* **12**(9): 094006. DOI: <http://dx.doi.org/10.1088/1748-9326/aa7def>.
- Scambos, T, Frezzotti, M, Haran, T, Bohlander, J, Lenaerts, J, Van Den Broeke, M, Jezek, K, Long, D, Urbini, S, Farness, K, Neumann, T, Alber, M, Winther, JG. 2012. Extent of low-accumulation 'wind glaze' areas on the East Antarctic plateau: Implications for continental ice mass balance. *Journal of Glaciology* **58**(210): 633–647. DOI: <http://dx.doi.org/10.3189/2012JoG11J232>.
- Schreiber, EAP, Serreze, MC. 2020. Impacts of synoptic-scale cyclones on Arctic sea-ice concentration: A systematic analysis. *Annals of Glaciology* **61**(82): 139–153. DOI: <http://dx.doi.org/10.1017/aog.2020.23>.
- Screen, JA, Simmonds, I. 2010. The central role of diminishing sea ice in recent Arctic temperature amplification. *Nature* **464**(7293): 1334–1337. DOI: <http://dx.doi.org/10.1038/nature09051>.
- Semmler, T, McGrath, R, Wang, S. 2012. The impact of Arctic sea ice on the Arctic energy budget and on the climate of the Northern mid-latitudes. *Climate Dynamics* **39**: 2675–2694. DOI: <http://dx.doi.org/10.1007/s00382-012-1353-9>.
- Serreze, MC, Barry, RG. 2011. Processes and impacts of Arctic amplification: A research synthesis. *Global and Planetary Change* **77**(1): 85–96. DOI: <http://dx.doi.org/10.1016/j.gloplacha.2011.03.004>.
- Shi, Y. 2019. Atmospheric Radiation Measurement (ARM) user facility. Surface meteorological instrumentation (PWD). 2019-10-11 to 2020-10-01, ARM mobile facility (MOS) MOSAIC (Drifting Obs—Study of Arctic Climate); AMF2 (M1). Compiled by Y. Shi [dataset]. ARM Data Center. DOI: <http://dx.doi.org/10.5439/1507725>. Accessed November 7, 2022.
- Shupe, MD, Rex, M, Blomquist, B, Persson, POG, Schmale, J, Uttal, T, Althausen, D, Angot, H, Archer, S, Bariteau, L, Beck, I, Bilberry, J, Bucci, S, Buck, C, Boyer, M, Brasseur, Z, Brooks, IM, Calmer, R, Cassano, J, Castro, V, Chu, D, Costa, D, Cox, CJ, Creamean, J, Crewell, S, Dahlke, S, Damm, E, de Boer, G, Deckelmann, H, Dethloff, K, Dütsch, M, Ebell, K, Ehrlich, A, Ellis, J, Engelmann, R, Fong, AA, Frey, MM, Gallagher, MR, Ganzeveld, L, Gradinger, R, Graeser, J, Greenamyre, V, Griesche, H, Griffiths, S, Hamilton, J, Heinemann, G, Helmig, D, Herber, A, Heuzé, C, Hofer, J, Houchens, T, Howard, D, Inoue, J, Jacobi, HW, Jaiser, R, Jokinen, T, Jourdan, O, Jozef, G, King, W, Kirchgaessner, A, Klingebiel, M, Krassovski, M, Krumpfen, T, Lampert, A, Landing, W, Laurila, T, Lawrence, D, Lonardi, M, Loose, B, Lüpkes, C, Maahn, M, Macke, A, Maslowski, W, Marsay, C, Maturilli, M, Mech, M, Morris, S, Moser, M, Nicolaus, M, Ortega, P, Osborn, J, Pätzold, F, Perovich, DK, Petäjä, T, Pilz, C, Pirazzini, R, Posman, K, Powers, H, Pratt, KA, Preußner, A, Quéléver, L, Radenz, M, Rabe, B, Rinke, A, Sachs, T, Schulz, A, Siebert, H, Silva, T, Solomon, A, Sommerfeld, A, Spreen, G, Stephens, M, Stohl, A, Svensson, G, Uin, J, Viegas, J, Voigt, C, von der Gathen, P, Wehner, B, Welker, JM, Wendisch, M, Werner, M, Xie, Z, Yue, F. 2022. Overview of the MOSAiC expedition: Atmosphere. *Elementa: Science of the Anthropocene* **10**(1). DOI: <http://dx.doi.org/10.1525/elementa.2021.00060>.
- Smith, DM. 1996. Extraction of winter total sea-ice concentration in the Greenland and Barents Seas from SSM/I data. *International Journal of Remote Sensing* **17**(13): 2625–2646. DOI: <http://dx.doi.org/10.1080/01431169608949096>.
- Spreen, G, Kaleschke, L, Heygster, G. 2008. Sea ice remote sensing using AMSR-E 89-GHz channels. *Journal of Geophysical Research: Oceans* **113**: C02S03. DOI: <http://dx.doi.org/10.1029/2005JC003384>.
- Spreen, G, Kern, S. 2017. Methods of satellite remote sensing of sea ice, in Thomas, DN ed., *Sea ice*. Chichester, UK: Wiley: 239–260. DOI: <http://dx.doi.org/10.1002/9781118778371.ch9>.
- Stroeve, J, Nandan, V, Willatt, R, Dadic, R, Rostosky, P, Gallagher, M, Mallett, R, Barrett, A, Hendricks, S, Tonboe, R, McCrystall, M, Serreze, M, Thielke, L, Spreen, G, Newman, T, Yackel, J, Ricker, R, Tsamados, M, Macfarlane, A, Hannula, HR, Schneebeli, M. 2022. Rain on snow (ROS) understudied in sea ice remote sensing: A multi-sensor analysis of ROS during MOSAiC (Multidisciplinary drifting Observatory for the Study of Arctic Climate). *The Cryosphere* **16**(10): 4223–4250. DOI: <http://dx.doi.org/10.5194/tc-16-4223-2022>.
- Svendsen, H, Mätzler, C, Grenfell, TC. 1987. A model for retrieving total sea ice concentration from

- a spaceborne dual-polarized passive microwave instrument operating near 90 GHz. *International Journal of Remote Sensing* **8**(10): 1479–1487. DOI: <http://dx.doi.org/10.1080/01431168708954790>.
- Thielke, L, Huntemann, M, Spreen, G.** 2022. Lead classification maps from helicopter-borne surface temperatures during the MOSAiC expedition. PANGAEA. DOI: <http://dx.doi.org/10.1594/PANGAEA.951569>.
- Tjernström, M, Shupe, MD, Brooks, IM, Persson, POG, Prytherch, J, Salisbury, DJ, Sedlar, J, Achtert, P, Brooks, BJ, Johnston, PE, Sotiropoulou, G, Wolfe, D.** 2015. Warm-air advection, air mass transformation and fog causes rapid ice melt. *Geophysical Research Letters* **42**(13): 5594–5602. DOI: <http://dx.doi.org/10.1002/2015GL064373>.
- Tonboe, R, Andersen, S, Toudal, L, Heygster, G.** 2006. Sea ice emission modelling applications, in Mätzler, C ed., *Thermal microwave radiation—Applications for remote sensing*. London, UK: The Institution of Engineering and Technology (IET): 382–400. (IET electromagnetic wave series; vol. 52). DOI: <http://dx.doi.org/10.1049/PBEW052E>.
- Tonboe, RT.** 2010. The simulated sea ice thermal microwave emission at window and sounding frequencies. *Tellus A* **62**(3): 333–344. DOI: <http://dx.doi.org/10.1111/j.1600-0870.2010.00434.x>.
- Tonboe, RT, Andersen, S, Toudal, L.** 2003. Anomalous winter sea ice backscatter and brightness temperatures. Copenhagen, Denmark: Danish Meteorological Institute. Scientific Report no: 03-13.
- Troitsky, AV, Osharin, AM, Korolev, AV, Strapp, JW.** 2003. Polarization of thermal microwave atmospheric radiation due to scattering by ice particles in clouds. *Journal of the Atmospheric Sciences* **60**(13): 1608–1620. DOI: [http://dx.doi.org/10.1175/1520-0469\(2003\)60<1608:POTMAR>2.0.CO;2](http://dx.doi.org/10.1175/1520-0469(2003)60<1608:POTMAR>2.0.CO;2).
- Ulaby, F, Long, D.** 2014. *Microwave radar and radiometric remote sensing*. Ann Arbor, MI: University of Michigan Press. DOI: <http://dx.doi.org/10.3998/0472119356>.
- Valkonen, E, Cassano, J, Cassano, E.** 2021. Arctic cyclones and their interactions with the declining sea ice: A recent climatology. *Journal of Geophysical Research: Atmospheres* **126**(12): e2020JD034366. DOI: <http://dx.doi.org/10.1029/2020JD034366>.
- Wagner, DN, Shupe, MD, Cox, C, Persson, OG, Uttal, T, Frey, MM, Kirchgassner, A, Schneebeli, M, Jaggi, M, Macfarlane, AR, Itkin, P, Arndt, S, Hendricks, S, Krampe, D, Nicolaus, M, Ricker, R, Regnery, J, Kolabutin, N, Shimanshuck, E, Oggier, M, Raphael, I, Stroeve, J, Lehning, M.** 2022. Snowfall and snow accumulation during the MOSAiC winter and spring seasons. *The Cryosphere* **16**(6): 2373–2402. DOI: <http://dx.doi.org/10.5194/tc-16-2373-2022>.
- Walbröl, A, Crewell, S, Engelmann, R, Orlandi, E, Griesche, H, Radenz, M, Hofer, J, Althausen, D, Maturilli, M, Ebell, K.** 2022. Atmospheric temperature, water vapour and liquid water path from two microwave radiometers during MOSAiC. *Scientific Data* **9**(1): 534. DOI: <http://dx.doi.org/10.1038/s41597-022-01504-1>.
- Wendisch, M, Brückner, M, Burrows, JP, Crewell, S, Dethloff, K, Ebell, K, Lüpkes, C, Macke, A, Notholt, J, Quaas, J, Rinke, A, Tegen, I.** 2017. Understanding causes and effects of rapid warming in the Arctic. *Eos* **98**(8): 22–26. DOI: <http://dx.doi.org/10.1029/2017EO064803>.
- Wendisch, M, Brückner, M, Crewell, S, Ehrlich, A, Notholt, J, Lüpkes, C, Macke, A, Burrows, JP, Rinke, A, Quaas, J, Maturilli, M, Schemann, V, Shupe, MD, Akansu, EF, Barrientos-Velasco, C, Bärfuss, K, Blechschmidt, AM, Block, K, Bougoudis, I, Bozem, H, Böckmann, C, Bracher, A, Bresson, H, Bretschneider, L, Buschmann, M, Chechin, DG, Chylik, J, Dahlke, S, Deneke, H, Dethloff, K, Donth, T, Dorn, W, Dupuy, R, Ebell, K, Egerer, U, Engelmann, R, Eppers, O, Gerdes, R, Gierens, R, Gorodetskaya, IV, Gottschalk, M, Griesche, H, Gryanik, VM, Handorf, D, Harm-Altstädter, B, Hartmann, J, Hartmann, M, Heinold, B, Herber, A, Herrmann, H, Heygster, G, Höschel, I, Hofmann, Z, Hölemann, J, Hünenbein, A, Jafariserajehlou, S, Jäkel, E, Jacobi, C, Janout, M, Jansen, F, Jourdan, O, Jurányi, Z, Kalesse-Los, H, Kanzow, T, Käthner, R, Kliesch, LL, Klingebiel, M, Knudsen, EM, Kovács, T, Körtke, W, Krampe, D, Kretzschmar, J, Kreyling, D, Kulla, B, Kunkel, D, Lampert, A, Lauer, M, Lelli, L, von Lerber, A, Linke, O, Löhnert, U, Lonardi, M, Losa, SN, Losch, M, Maahn, M, Mech, M, Mei, L, Mertes, S, Metzner, E, Mewes, D, Michaelis, J, Mioche, G, Moser, M, Nakoudi, K, Neggens, R, Neuber, R, Nomokonova, T, Oelker, J, Papakonstantinou-Presvelou, I, Pätzold, F, Pefanis, V, Pohl, C, van Pinxteren, M, Radovan, A, Rhein, M, Rex, M, Richter, A, Risse, N, Ritter, C, Rostosky, P, Rozanov, VV, Donoso, ER, Garfias, PS, Salzmann, M, Schacht, J, Schäfer, M, Schneider, J, Schnierstein, N, Seifert, P, Seo, S, Siebert, H, Soppa, MA, Spreen, G, Stachlewska, IS, Stapf, J, Stratmann, F, Tegen, I, Viceto, C, Voigt, C, Vountas, M, Walbröl, A, Walter, M, Wehner, B, Wex, H, Willmes, S, Zanatta, M, Zeppenfeld, S.** 2023. Atmospheric and surface processes, and feedback mechanisms determining Arctic amplification: A review of first results and prospects of the (AC)³ project. *Bulletin of the American Meteorological Society* **104**(1): E208–E242. DOI: <http://dx.doi.org/10.1175/BAMS-D-21-0218.1>.
- Wever, N, Rossmann, L, Maaß, N, Leonard, KC, Kaleschke, L, Nicolaus, M, Lehning, M.** 2020. Version 1 of a sea ice module for the physics-based, detailed, multi-layer SNOWPACK model. *Geoscientific Model Development* **13**(1): 99–119. DOI: <http://dx.doi.org/10.5194/gmd-13-99-2020>; <https://gmd.copernicus.org/articles/13/99/2020/>.
- Wiesmann, A, Mätzler, C.** 1999. Microwave emission model of layered snowpacks. *Remote Sensing of Environment* **123**(3): 307–316. DOI: [http://dx.doi.org/10.1016/S0034-4257\(99\)00046-2](http://dx.doi.org/10.1016/S0034-4257(99)00046-2).

Woods, C, Caballero, R. 2016. The role of moist intrusions in winter Arctic warming and sea ice decline. *Journal of Climate* **29**(12): 4473–4485. DOI: <http://dx.doi.org/10.1175/JCLI-D-15-0773.1>.

Woods, C, Caballero, R, Svensson, G. 2013. Large-scale circulation associated with moisture intrusions into the Arctic during winter. *Geophysical Research*

Letters **40**(17): 4717–4721. DOI: <http://dx.doi.org/10.1002/grl.50912>.

Zhang, P, Chen, G, Ting, M, Ruby Leung, L, Guan, B, Li, L. 2023. More frequent atmospheric rivers slow the seasonal recovery of Arctic sea ice. *Nature Climate Change* **13**: 1–8. DOI: <http://dx.doi.org/10.1038/s41558-023-01599-3>.

How to cite this article: Rückert, JE, Rostosky, P, Huntemann, M, Clemens-Sewall, D, Ebell, K, Kaleschke, L, Lemmetyinen, J, Macfarlane, AR, Naderpour, R, Stroeve, J, Walbröl, A, Spreen, G. 2023. Sea ice concentration satellite retrievals influenced by surface changes due to warm air intrusions: A case study from the MOSAiC expedition. *Elementa: Science of the Anthropocene* 11(1). DOI: <https://doi.org/10.1525/elementa.2023.00039>

Domain Editor-in-Chief: Jody W. Deming, University of Washington, Seattle, WA, USA

Guest Editor: Wieslaw Maslowski, Oceanography, Naval Postgraduate School, Monterey, CA, USA

Knowledge Domain: Ocean Science

Part of an Elementa Special Feature: The Multidisciplinary Drifting Observatory for the Study of Arctic Climate (MOSAIC)

Published: December 15, 2023 **Accepted:** October 09, 2023 **Submitted:** March 10, 2023

Copyright: © 2023 The Author(s). This is an open-access article distributed under the terms of the Creative Commons Attribution 4.0 International License (CC-BY 4.0), which permits unrestricted use, distribution, and reproduction in any medium, provided the original author and source are credited. See <http://creativecommons.org/licenses/by/4.0/>.

